AFRL-SR-AR-TR-04-

0356

REPORT DOCUMENTATION PAGE

1. REPORT DATE *(DD-MM-YYYY)*	2. REPORT TYPE	3. DATES COVERED *(From - To)*
04-05-2004	Final Report	04-01-2000 03-31-2003

4. TITLE AND SUBTITLE
INVESTIGATION OF COMBINED LOW-ANGLED JETS AND VARIABLE WALL GEOMETRY FOR HYPERSONIC AERODYNAMIC CONTROL

5a. CONTRACT NUMBER
F49620-00-1-0329

5b. GRANT NUMBER

5c. PROGRAM ELEMENT NUMBER

6. AUTHOR(S)
Rodney D. W. Bowersox, Dr.

Charles L. Karr, Dr., Muhammad Sharif, Dr.

5d. PROJECT NUMBER

5e. TASK NUMBER

5f. WORK UNIT NUMBER

7. PERFORMING ORGANIZATION NAME(S) AND ADDRESS(ES)
The University of Alabama
Aerospace Engr. & Mechanics
Box 870280
Tuscaloosa, AL 35487

8. PERFORMING ORGANIZATION REPORT NUMBER
UA-AEM-APL-2000-001

9. SPONSORING / MONITORING AGENCY NAME(S) AND ADDRESS(ES)
AFOSR
4015 Wilson Boulevard
Room 713
Arlington VA 22203-1954

10. SPONSOR/MONITOR'S ACRONYM(S)

11. SPONSOR/MONITOR'S REPORT NUMBER(S)

12. DISTRIBUTION / AVAILABILITY STATEMENT
Approved for Public Release; Distribution Unlimited

13. SUPPLEMENTARY NOTES

14. ABSTRACT

The principal objective of the present research proposal was to investigate, experimentally and numerically, the use of jets to actively control the aerodynamic forces for high-speed flight vehicles. As a test bed, single port injection into a Mach 5.0 crossflow through diamond and circular orifices, at various incidence angles and momentum ratios were examined. To meet the objective, a research program was performed to characterize and control the secondary flow structures associated with the jet interaction flows. The research approach was divided into three main thrusts. First, fundamental studies to characterize the mean and turbulent flow structure were performed. This included detailed experiments at Mach 5.0 using advanced optical diagnostics and numerical simulations using two-equation RANS turbulence modeling. The flow field characterization included shock structures, surface pressure, vorticity and turbulence. Second, the numerical simulations were studied to assess vorticity and turbulent transport mechanisms. Lastly, parametric experiments and Reynolds averaged Navier-Stokes simulations were performed to quantify vorticity control. This included manipulating the jet shock structure to modify the vorticity field, adding downstream ramps to utilize the Magnus force, varying the injector geometry, incidence angle and momentum ratio.

15. SUBJECT TERMS
Hypersonic Flow, Jet-Into-A-Cross-flow, Reaction Control, Vorticity, Fuel Injection

16. SECURITY CLASSIFICATION OF:			17. LIMITATION OF ABSTRACT	18. NUMBER OF PAGES	19a. NAME OF RESPONSIBLE PERSON
a. REPORT	b. ABSTRACT	c. THIS PAGE			Rodney Bowersox
Unclassified	Unclassified	Unclassified	SAR		19b. TELEPHONE NUMBER *(include area code)* (205)348-1905

Standard Form 298 (Rev. 8-98)
Prescribed by ANSI Std. Z39.18

20040715 134

RECEIVED MAY 14 2004

TAMU-AE-APR-2004-001
MAY 5 2004

INVESTIGATION OF COMBINED LOW-ANGLED JETS AND VARIABLE WALL GEOMETRY FOR HYPERSONIC AERODYNAMIC CONTROL

F49620-00-1-0329

FINAL REPORT

Dr. Rodney D. W. Bowersox
Department of Aerospace Engineering
701 H.R. Bright Bldg, 3141 TAMU
Texas A&M University
College Station, TX 77845

Drs. Charles L. Karr and Muhammad A.R. Sharif
Aerospace Engineering and Mechanics
Box 870280
Tuscaloosa, AL 35487-0280

Executive Summary

The principal objective of the present research proposal was to investigate, experimentally and numerically, the use of jets to actively control the aerodynamic forces for high-speed flight vehicles. As a test bed, single port injection into a Mach 5.0 crossflow through diamond and circular orifices, at various incidence angles and momentum ratios were examined. To meet the objective, a research program was performed to characterize and control the secondary flow structures associated with the jet interaction flows. The research approach was divided into three main thrusts. First, fundamental studies to characterize the mean and turbulent flow structure were performed. This included detailed experiments at Mach 5.0 using advanced optical diagnostics and numerical simulations using two-equation RANS turbulence modeling. The flow field characterization included shock structures, surface pressure, vorticity and turbulence. Second, the numerical simulations were studied to assess vorticity and turbulent transport mechanisms. Lastly, parametric experiments and Reynolds averaged Navier-Stokes simulations were performed to quantify vorticity control. This included manipulating the jet shock structure to modify the vorticity field, adding downstream ramps to utilize the Magnus force, varying the injector geometry, incidence angle and momentum ratio.

The Air Force Research Laboratory High-Speed Propulsion Division is investigating the use of diamond jets for supersonic combustion ramjet (scramjet) primary fuel injectors.

The results of this research program include a new experimental and numerical database for sonic injection into a Mach 5.0 crossflow and new understanding of the vorticity dynamics for this flow. The results were disseminated to the US Air Force and aerospace industry through this contractor report, archival journal publications and presentations at national conferences.

The lead PI for this project was Dr. Rodney D. W. Bowersox, Associate Professor of Aerospace Engineering at Texas A&M University. He moved to Texas A&M University during the second year of the project, and the project remained at The University of Alabama under the co-PI Dr. Charles L. Karr. Dr. Muhammad A. R. Sharif was the third co-PI on this project. The Mach 5.0 wind tunnel tests and numerical simulations were carried out by Dr. Bowersox and his graduate students Huaiguo Fan (PhD, currently on the faculty at the Chongqing University), Daina Lee (MS, currently at ATA, Inc. at AEDC) and Ravichandra Srinivasan (currently a PhD candidate at Texas A&M). Drs. Karr and Sharif performed the design optimization studies. Although, unfunded, Dr. Bowersox continued the numerical simulations at Texas A&M University. In addition, he is currently performing detailed high-fidelity simulation under an Air Force supercomputer grant on the Air Force ASC HPC; the results from these simulations will be reported at a later date.

Table of Contents

List of Symbols

A_j	Injector Exit Port Area
A_p	Plume Area
d	Effective Jet Diameter for the Single-Port-Injector [$=(4A_j/\pi)^{1/2} = 4.89$ mm]
d_d	Effective Jet Diameter for the Distributed-Array-Injector (= 2.2 mm)
J	Jet-to-Free stream Momentum Ratio ($=\rho_j u_j^2/\rho_\infty u_\infty^2$)
M	Mach Number
p	Static Pressure
p_{eff}	Effective Back Pressure
p_t	Total Pressure
R	$= \rho_j u_j/\rho_\infty u_\infty$
Re/m	Unit Reynolds Number
T	Static Temperature
T_t	Total Temperature
u	Axial Velocity
x, y, z	Cartesian Coordinates
y_{max}	Maximum Plume Penetration
α	Injector Incidence Angle
ρ	Density
τ_{ij}^T	Turbulent Shear Stress

Subscripts

j	Injector Condition
∞	Free Stream Condition
1	Flow Condition Upstream Shock
2	Flow Condition Downstream of Shock

Chapter 1

Introduction

1.1 Documented Air Force Requirements

The U.S. Air Force requirements for hypersonic vehicles, and the technical challenges thereof, are clearly outlined in (1) the *New World Vista's* document (1995), (2) the *System Concepts and Technology Development of Operationally Responsive Reusable Military Aerospace Vehicle* paper [Dolvin (2002)], and (3) the *Unsteady Aerodynamics and Hypersonics* section of the AFOSR BAA [Schmisseur (2003)]. In summary, "sustained hypersonic flight offers potential revolutionary improvements in future war-fighting and space launch capabilities. ... Hypersonic speeds greatly enhance both survivability and lethality by practically eliminating enemy defensive capabilities. (*New World Vistas*, 1995)." Potential future Air Force vehicles include space launch support accelerators, missiles, maneuvering re-entry vehicles, and rapid-response global-reach aircraft systems.

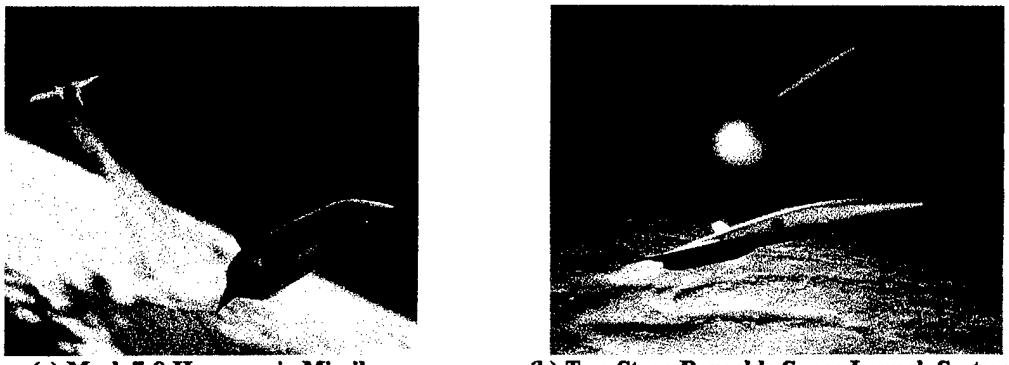

(a) Mach 7-8 Hypersonic Missile **(b) Two Stage Reusable Space Launch System**

Fig. 1.1 Example Air Force Hypersonic Vehicles [Erbland (2002)]

Many of the advanced hypersonic vehicle concepts, such as those in Fig. 1.1, are envisioned to use complex combined engines and/or perform rapid maneuvers, such as that shown in Fig. 1.2

Fig. 1.2 Generic Scramjet Engine

High-speed jet interaction flows, as shown in Fig. 1.3, have numerous potential applications for the vehicles shown in Fig. 1.1. For example jets can be very effective rapid reaction control devices for hypersonic vehicles. One advantage of a reaction control jet over a control surface is the elimination of a thermally protected control surface. However, jet interaction flows are turbulent (see Fig. 1.3a) and they are characterized by numerous complicated vortical flow features, as depicted in Fig. 1.3b. Thus, modern physical models are not accurate. Jet flows and prediction limitation are described in more detail in Chapter 2.

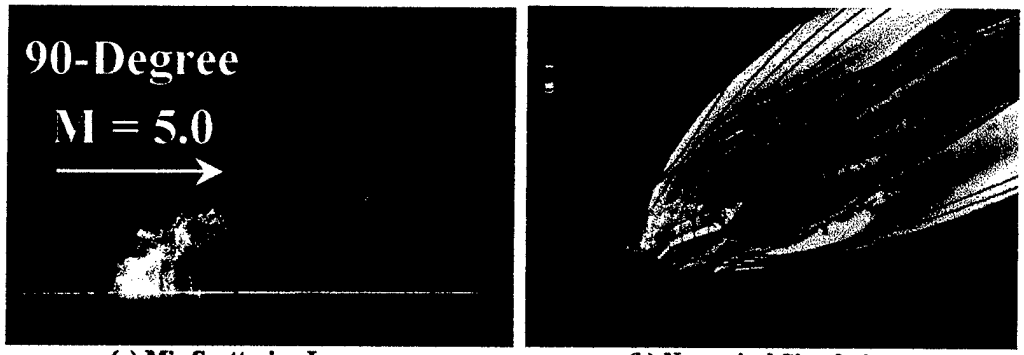

(a) Mie Scattering Image (b) Numerical Simulation

Fig. 1.3 Sonic Injection into a Mach 5 Cross Flow [Present Study]

Jets are also effective for film cooling thermal protection. A Mach 8 vehicle will experience wall temperatures on the order of 2,700K. The only metals that can survive these temperatures are very heavy (e.g., Tungsten is nearly ten times heavier than Titanium). Thus, the aerosurfaces will require thermal protection (either ceramics or film cooling). One of the distinguishing characteristics of a jet into a cross-flow is the strong counter-rotating vortex pair within the plume (see Chapter 2 for a detailed flow field description). This counter rotating vortex pair has an adverse influence on the film cooling effectiveness, where the vortex pair interacts with the surface causing the jet plume to lift-off the surface via the Magnus force. In a recent study aimed at improving the penetration of a jet into a supersonic cross-flow, our group investigated the use of small ramps placed just downstream of the injector port [Wilson, Bowersox and Glawe (1998)]. The ramps were designed to interact with the counter-rotating vortex pair, and thus increase the penetration via the Magnus force. Our team discovered that by varying the ramp geometry the plume vorticity could be controlled. One ramp configuration reduced the vorticity within the plume to the level of being undetectable, and our

numerical simulations [Chenault, Beran and Bowersox (1999)] indicated that the recompression shock (described in Chapter 2) is a main vorticity production mechanism. Hence, the most likely case for the plume vorticity control is that the ramps reshape the recompression shock. Once the flow processes are better understood, methodologies that range from simple fixed ramps to sophisticated nonlinear adaptive control using micro-electrical-mechanical systems (MEMS) can be developed to control the jet plume features including plume axial vorticity.

Although the counter-rotating vortex pair can have a negative impact on film cooling, this characteristic has the potential to be an effective means of boundary layer control. It is expected that the axial vorticity within the jet plume can be used to energize the lower portion of the boundary layer with the goal of reducing wall pressure fluctuations by extending the axial length of the "U-vortex" described in Hinze (1975). Low-speed experimental data indicate that the wall shears stress is linearly proportional to the root-mean-square wall pressure fluctuations (Hinze, 1975). Hence, the reduced wall pressure fluctuations will result in reduced momentum loss (skin friction). Energizing the boundary layer can also be used to increase the resistance of the boundary layer to shock induced separation. These include reaction control, separation control, shock interaction control and fuel injection for the scramjet engine as shown in Fig. 1.2.

In summary, the understanding and predictability of a jet into a cross-flow, especially at high-speeds, is limited by the extreme dearth of experimental studies (Chapter 2 describes in detail the current limitations). However, as discussed Chapter 2, recent advances in experimental methods allow for in depth studies directed at

understanding the flow physics. The better flow field understanding, produced in this study, provides engineers and scientists the requisite information to capitalize on the jet flow features to enhance the performance of hypersonic systems.

1.3 Research Objectives and Approach

The principal objective of the present research proposal is to investigate, experimentally and numerically, the use of jets to actively control the aerodynamic forces for high-speed flight vehicles. As a test bed, single port injection into a Mach 5.0 crossflow through diamond and circular orifices, at various incidence angles and momentum ratios were examined. To meet the objective, a research program was performed to characterize and control the secondary flow structures associated with the jet interaction flows. The research approach was divided into three main thrusts. First, fundamental studies to characterize the mean and turbulent flow structure were performed. This included detailed experiments at Mach 5.0 using advanced optical diagnostics and numerical simulations using two-equation RANS turbulence modeling. The flow field characterization included shock structures, surface pressure, vorticity and turbulence. Second, the numerical simulations were studied to assess vorticity and turbulent transport mechanisms. Lastly, parametric experiments and Reynolds averaged Navier-Stokes simulations were performed to quantify vorticity control. This included manipulating the jet shock structure to modify the vorticity field, adding downstream ramps to utilize the Magnus force, varying the injector geometry, incidence angle and momentum ratio.

1.4 Scientific Impact and Technology Transitions

The Air Force Research Laboratory High-Speed Propulsion Division is investigating the use of diamond jets for supersonic combustion ramjet (scramjet) primary fuel injectors.

1.5 Deliverables

The results of this research program include a new experimental and numerical database for sonic injection into a Mach 5.0 crossflow and new understanding of the vorticity dynamics for this flow. The results were disseminated to the US Air Force and aerospace industry through this contractor report, archival journal publications and presentations at national conferences.

1.6 Personnel

The lead PI for this project was Dr. Rodney D. W. Bowersox, Associate Professor of Aerospace Engineering at Texas A&M University. He moved to Texas A&M University during the second year of the project, and the project remained at The University of Alabama under the co-PI Dr. Charles L. Karr. Dr. Muhammad A. R. Sharif was the third co-PI on this project. The Mach 5.0 wind tunnel tests and numerical simulations were carried out by Dr. Bowersox and his graduate students Huaiguo Fan

(PhD, currently on the faculty at the Chongqing University), Daina Lee (MS, currently at ATA, Inc. at AEDC) and Ravichandra Srinivasan (currently a PhD candidate at Texas A&M). Drs. Karr and Sharif performed the design optimization studies.

1.7 Publication Summary (*indicates student under the direction of Dr. Bowersox)

Bowersox, R., Fan,* H., and Lee,* D., "Sonic Injection into a Mach 5.0 Freestream through Diamond Orifices," *Journal of Propulsion and Power*, Vol. 20, No. 2, 2004, pp. 280-287.

Srinivasan,* R. and Bowersox, R. "Use of Transverse Injection for Hypersonic Flow Control," AIAA-2004-2698, 2nd AIAA Flow Control Conference, Portland, Oregon Jun 28 - Jul 1, 2004.

Bowersox, R., Fan*, H., and Lee*, D., "Sonic Injection into a Mach 5.0 Freestream through Diamond Shaped Orifices at Various Incidence," AIAA-2003-5190, AIAA/ASME/SAE/ASEE Joint Propulsion Conference, Huntsville, AL, July 2003.

Srinivasan*, R. and Bowersox, R., "Numerical Analyses of Gaseous Injection into a Mach 5.0 Freestream through Diamond Orifices," AIAA-2003-5188, AIAA/ASME/SAE/ASEE Joint Propulsion Conference, Huntsville, AL, July 2003.

Fan*, H. and Bowersox, "Gaseous Injection through Diamond Orifices at Various Incidence Angles into a Hypersonic Freestream," AIAA 2001-1050, 39th AIAA Aerospace Sciences Meeting, Reno NV, Jan 2001.

Chapter 2

Jet-Interaction Background Review

2.1 Jet-Into-A-Cross-flow

Injection into a cross-flow is a fundamentally important flow field that has implications across a myriad of military and civil disciplines. Thus, numerous experimental studies, primarily at low-speeds, have been performed to quantitatively assess the mean flow field and qualitatively examine the instantaneous vortical flow features [for example, Margason (1993), Kuethe (1935), and Kamotani and Greber (1972)]. However, studies that contain turbulence data suitable for flow field understanding are exceedingly scarce [Margason (1993)]. Furthermore, the available mean and turbulence data for supersonic flows are also limited. However, some studies were found, and the results of which are integrated into the following the discussions. Hypersonic jet-interaction studies are virtually non-existent.

Injection into a low-speed cross-flow produces a complex flow with at least four distinguishable vortical flow characteristics (see Fig. 2.1). As the jet emerges into the cross-flow, it is curved downstream by the cross-flow. The jet plume cross-section evolves into a cardioidal or "kidney-bean" shape. The counter-rotating vortex pair within the plume is responsible for the distorted plume shape. A number of flow mechanisms are responsible for generating this secondary flow. For example, turning of the flow into the downstream direction creates a pressure gradient across the flow that induces vortical motion. Lateral shearing along the plume edges also contributes to the vorticity. The jet-

free stream interaction (separation) creates a horseshoe vortex similar to that of a wing-body junction on an aircraft. The third vortex system consists of jet-shear layer vortices. Lastly, a fourth wake vortex system exists. Until recently, the formation of this unsteady vortex phenomenon had been attributed to vortex shedding similar the Karman-vortex wake of a cylinder in a cross-flow. Because Fric and Roshko (1994) were only able to visualize this system when the boundary layer was seeded with smoke, they reasoned that the vortices were the result of upstream boundary layer vorticity being transported up into the wake. The process is believed to be the result of "separation events" and eruptions of the boundary layer fluid and vorticity into "tornado-like" structures that begin at the wall and are entrained into the jet flow. Although Fric and Roshko present rather convincing evidence for this hypothesis, some contradicting evidence has also been presented. For example, the planar laser induced fluorescence concentration measurements of Lozano et al. (1994), show signs of the structures. However in that study, only the jet flow was seeded. Hence, these data may suggest that these structures could in part emanate from the jet and not the wall. Adding to this apparent dilemma, Kelso et al. (1993) present three possible scenarios leading to the formation of the wake vortex system. These unsteady phenomena can be very important for future flow control algorithms.

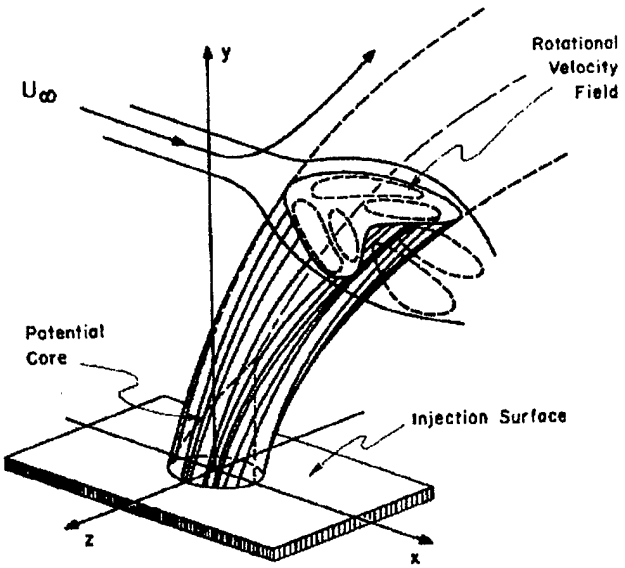

Fig. 2.1 Low-Speed Jet-Interaction Schematic [Abromovich (1960)]

For high-speed flows, the mean flow features are similar to those described above. However, compressibility creates additional features that do not have incompressible counterparts. For example, perpendicular injection of an underexpanded sonic or supersonic jet into a supersonic free stream produces several flow structures. The first of these is a bow shock produced as the free stream impacts the injection streamtube; in this respect the injectant acts as a solid cylindrical body [Hollo, McDaniel and Hartfield (1994)]. For injector configurations where injector diameter is greater than the boundary layer thickness, a separation bubble and a lambda shock form slightly upstream of the injector port [Schetz and Billig (1966)]. After entering the free stream, the jet experiences a rapid Prandtl-Meyer expansion (usually assumed to be an isentropic process) surrounded by a barrel shock [Grasso and Magi (1995)]. A shock normal to the jet path, known as the Mach disk, terminates the barrel shock, and compresses the flow to

the appropriate (i.e., effective) back pressure. As the free stream flow wraps around the jet, a recompression shock is created. Recent CFD calculations by our team [Chenault, Beran and Bowersox (1999)] (see Fig. 2.2) indicate that the recompression shock creates an addition counter-rotating vortex pair that eventually engulfs the original jet induced pair discussed above.

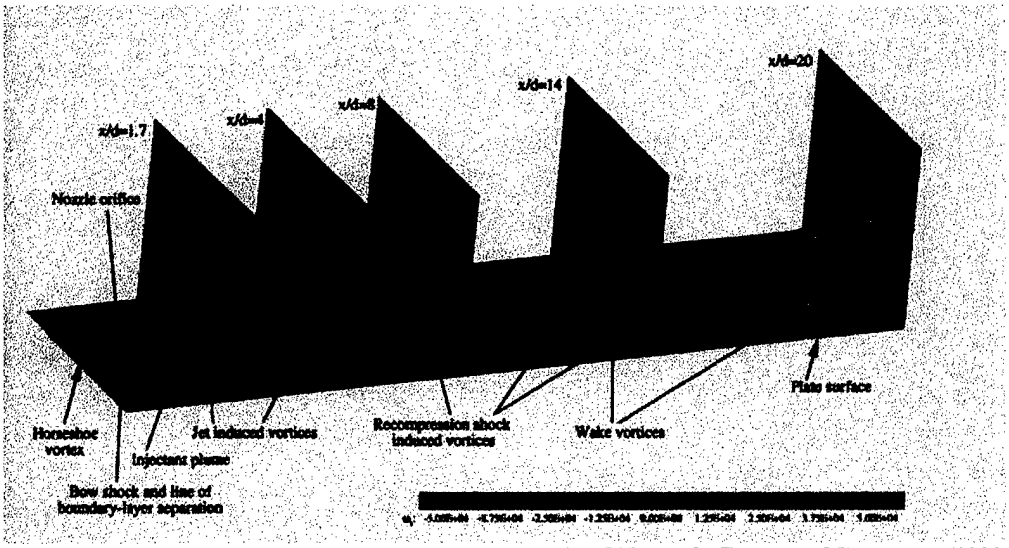

Fig. 2.2 High-Speed Jet-Interaction Vorticity Distribution [Chenault, Beran and Bowersox (1999)]

Angled injection is a means of reducing total pressure loss. In either normal or angled injection, the entry of the injectant jet into the mainstream flow can be regarded as a two-stage process [Schetz and Billig (1966)]. The jet first enters the main flow and remains relatively intact as it expands to the height of the Mach disk. Beyond the Mach disk, the flow turns coaxial to, and accelerates with, the main flow. In the second stage, the jet acts as a coaxial vortex mixing structure. It is this feature that may be useful for boundary layer control (i.e., drag reduction).

During a rather extensive literature review, only a very limited number of studies

on injection flows were found that included turbulence measurements. For low-speed flows Andreopoulus and Rodi (1984), Fric and Roshko (1989), Kamotani and Greber (1972) were the only ones identified. For high-speed flows, the McCann and Bowersox (1996) and Bowersox (1996c) Mach 3.0 studies were the only ones located. This finding is consistent with that of the Margason (1993). Hence, the turbulent flow physics of the injection into a cross-flow are significantly less understood than their mean flow counterpart. However from the available data, some limited qualitative insight into the overall structure can be gleaned. For example the axial turbulence intensity contour plots of Kamotani and Greber (1972) indicated that two peaks in the intensity levels existed across the plume. In addition, the peaks were roughly co-located with each of the vortices of the counter rotating vortex pair. Investigating a high-speed angled injection case, McCann and Bowersox (1996) found that the turbulent kinetic energy also had two peaks, which were roughly, located just below each vortex with the vortex pair. They deduced that the increased strain rates due to the secondary vortex flow resulted in an increased production of the turbulent kinetic energy. The data of McCann and Bowersox also demonstrated that the x-y turbulent shear stresses peaked along the plume centerline, and the x-z shear stresses were highly asymmetrical. However, as suggested by Cantwell (General Discussion, 1993), the peak turbulence levels along the jet centerline may be the result of an unsteady movement of the vortex pair. It is also important to mention here that a number of experimental studies show an asymmetry in the mean flow. Further, the numerical simulation of a shocked jet (Drummond, 1996) also showed signs of an asymmetry. Bowersox (1996c) presents three possible scenarios to explain the

generation of the asymmetry. The incompressible data of Andreopoulus and Rodi (1984) presented the axial variation of the x-y and x-z turbulent shear stresses for two spanwise locations. Unfortunately, the spatial resolution of that study was sparse; hence, only limited quantitative information was available. However, those data showed trends in the turbulence decay rates. Though the limited data available in the literature, in conjunction with a current understanding of the mean flow field, can provide a qualitative impression of the turbulent flow structure, studies with enough detail for turbulence model development and validation are virtually non-existent. This conclusion is supported by the review of Margason (1993), and it was also the consensus during the General Discussion session following a recent AGARD meeting (General Discussion, 1993) among a number of key international researchers. Further, Chui et. al. (1993) and Alverez et al. (1993) both indicated that turbulence modeling was the limiting key factor in determining the accuracy of their numerical predictions. Hence, detailed experimental studies are required to develop turbulence models for design applications.

2.2 Overview of Current Prediction Methods and Empirical Database

Currently, engineers and scientists rely on an approximate form the governing equations of motion to predict the overall mean flow character of these flows. The Reynolds and Favre averaged forms of the Navier-Stokes equations are universally used to compute low-speed and high-speed flows, respectively.

Associated with the averaging procedure is the requirement for accurate turbulence models. Currently, industry standard eddy viscosity gradient transport

turbulence models, such as Baldwin-Lomax algebraic and k-ε/ω two equation, are extended to more complex flows on an *ad hoc* basis. However, as discussed in Wilcox (1993), current eddy viscosity models are not accurate for three-dimensional, vortex-dominated flows. As discussed in Section 2.1, the jet into a cross-flow flow field is dominated by numerous three-dimensional vortex systems; thus, the current prediction methods are not accurate.

In a recent numerical study of injection into a cross-flow, Chui et al. (1993) noted that the predictions of the flow with the eddy viscosity Baldwin-Lomax and Baldwin-Barth models "... compared no better with the experimental data than the laminar flow computation." Alverez et al. (1993) reported similar shortcomings. In a recent survey of 333 articles that covered a 50-year era, Margason (1993) concluded that there is a need for high quality, high fidelity experimental data that will allow for verification of current and future computational fluid dynamic results and to define the unsteady flow characteristics. Also, the during the General Discussion, following the 1993 AGARD (General Discussion, 1993) conference, entitled *Computational and Experimental Assessment of Jets in a Cross-flow,* there was some surprise that more detailed and high fidelity Laser Doppler and Particle Image Velocimetry data were not available for turbulence model development and evaluation.

2.3 Recent Advances in Technology that Allow for the Present Research

Modern advanced laser based experimental diagnostic techniques, such as particle image velocimetry and pressure sensitive paint, allow for detailed and accurate

measurements of the instantaneous mean, and turbulence statistics at high spatial resolution. In addition, modern computational resources, such as the University of Alabama Super Computer (described in Chapter 3), allow for routine simulation of complex three-dimensional flows.

2.4 Control of the Jet into a Cross-flow Using Variable Wall Geometry

In a recent research program focused on supersonic combustion applications, Wilson, Bowersox and Glawe (1998) placed small ramps just downstream of the exit port of a jet issuing into a high-speed cross-flow. The original motivation behind placing the ramps was to increase penetration via the Magnus force generated by interaction between the strong counter rotating vortex pair within the plume (Section 2.1 describes the flow features) and the ramp surfaces. That study was limited to one injector angle (25 degrees) at Mach 3.0. However, seven ramp configurations were tested. Because of the lack of design tools (i.e., suitable turbulence models), the ramps were designed based on intuitive arguments. The effects of the small ramps on the plume structure were significantly more pronounced than expected, and they were strongly dependent on the ramp geometry. For one particular ramp, the normally very strong counter rotating vortex pair (20,000-30,000 /s) was reduced in strength to the point of being undetectable with laser based Mie scattering experimental apparatus. On the other hand, a second ramp configuration produced stronger vortices within the plume. The aforementioned lack of understanding of the flow physics made determining the physical mechanisms responsible for the effects of the ramps on the plume structure unattainable. However,

the recent simulations of Chenault, Beran and Bowersox (1999) indicated that the recompression shock is a main vorticity production mechanism. Hence, the most likely case for the plume vorticity control is that the ramps reshape the recompression shock. Once these flow processes are better understood, methodologies that range from simple fixed ramps to sophisticated nonlinear adaptive control using micro-electrical-mechanical systems (MEMS) can be developed to control the jet plume features (e.g., shape, trajectory and unsteady, three-dimensional nonlinearities). Thus, optimizing the performance of numerous engineering endeavors.

Chapter 3

Facilities and Apparatus Development

This section provides a detailed description of the facility and apparatus development work that was accomplished in the research program.

3.1 Wind Tunnels

3.1.1 Mach 5.0 Wind Tunnel

A Mach 5.0 blow-down tunnel with a 6.0 second run time was used for the present study. The free stream Mach number was measured as 4.9 with a ±2% variation across the test section core flow. The operating conditions are listed in Table 3.1. A schematic of the wind tunnel, along with a photograph, is given in Fig. 3.1.

Table 3.1 Freestream Flow Conditions

Mach	P_t (MPa)	T_t (K)	Re/m (x10^6)	δ (mm)
4.95±2.0%[a]	2.40±4.0%[b]	360±3.0%[b]	53.	7.6±7.0%[c]

[a]Variation across the freestream, [b]Held constant to within this amount,
[c]Variation across the tunnel span

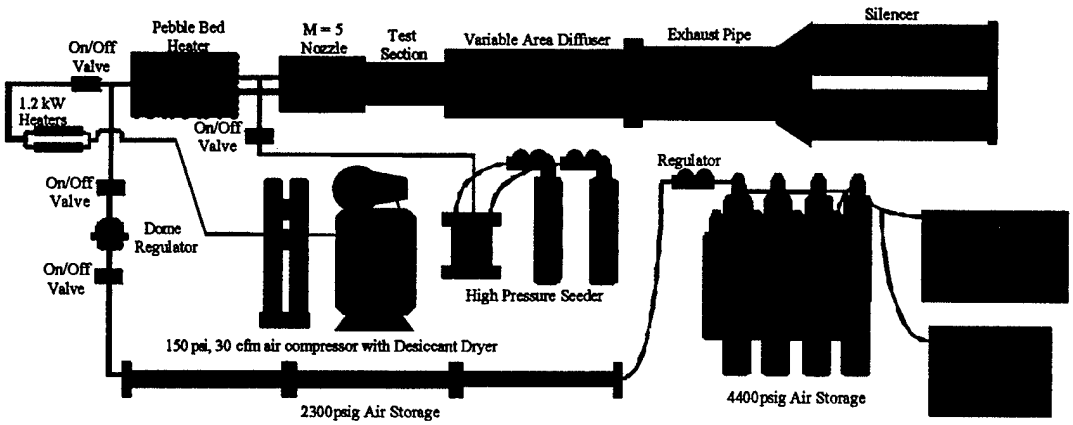

(a) Facility Schematic

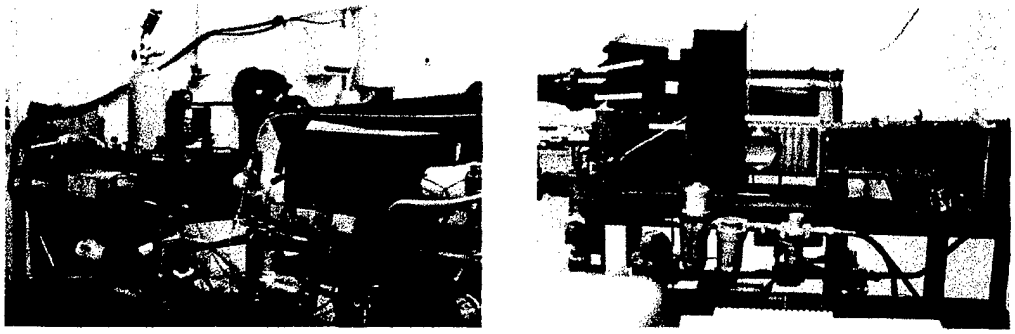

(b) Photographs

3.1 Mach 5.0 Wind Tunnel

The high-pressure air supply pumping system was a Hypres Air System Model HP-6000-NA4-E3 four-stage, reciprocating air-cooled air compressor, which was driven by a 7.46 kW (10 hp), 230 VAC Marathon Electric motor. This system provides a flow rate of 5.66 liter/s (12 cfm). The air from the compressor was cooled and dried by inerstage coolers and separators, and purifier desiccant cartridges. The system provided grade E breathing air [CO < 10 ppm v/v, CO_2 < 500 ppm v/v, total hydrocarbon content < 25 ppm v/v, oil (condensable mist/vapor) < 5 ppm w/v] with a dew point of -45 °C [63 ppm v/v (0.05 mg/l)]. The 30 MPa (4400 psia) high-pressure air was stored in eight DOT

air bottles, each with a volume of 0.058 m^3. The time to compress from atmospheric to full capacity was approximately four hours, and a full supply of air was sufficient for nominally four wind tunnel runs. A second Hypres Brand HP-6000-NA3-E3 three-stage compressor system was purchased. This three-stage system is very similar to the above-described four-stage system. The system, which driven by a 5.59 kW (7.5 hp) motor provides an additional 4.25 liter/sec (9 cfm) grade E air.

Because the mass flow rate for the tunnel exceeded that available directly from the bottle farm, the air for single run was transferred to an intermediate tank for temporary storage and high volume blow-down. The intermediate tank consisted of three 6.0 m sections of 10.16 cm (4 inch) diameter schedule 120 stainless pipe. The tank volume was 0.11 m^3, and the intermediate pressure was set at 15.9 MPa (2,300 psia). The air from the intermediate tank flowed to the tunnel through a 2.54 cm (1.0 inch) stainless steel tube. Two Grove Model 302G Pressure Reducing regulators, located in series, regulated the pressure of the air entering the wind tunnel to within ±2% of the desired pressure. The dome pressure for the first regulator was set at 5.86 MPa (850 psia) and the second was set 5.17 MPa (750 psi). These settings overcame the pressure drop in the system (plumbing and pebble bed heater) to provide a total pressure at the nozzle of 2.34 MPa (340 psi).

To prevent oxygen liquefaction, a pebble bed was designed to heat the air before entering the nozzle. The pebble bed heating system was designed and constructed in-house for this project. A rectangular (interior dimensions of 12.7 x 12.7 x 49.53 cm^3) high temperature grade stainless steel (RA321) vessel held the pebble bed. The pressure

vessel was constructed from 5.08 cm thick plates, and was pressure tested with hydraulic oil to 17.24 MPa (2500 psi). Shown in Fig. 3.2 is a photograph of the pebble bed. The pebble bed consisted of stainless steel (316) pebbles with diameter of 6.35mm each. The pebbles absorbed thermal energy when low-pressure heated air flowed through.

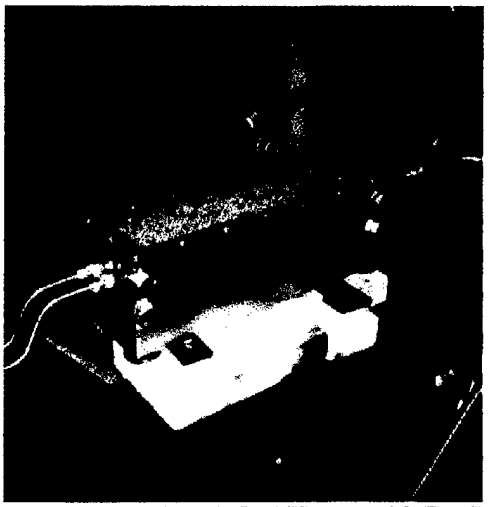

Fig. 3.2 Photographs of Pebble Bed Heater with Top Removed

The pebbles were heated with two Reheat Brand model PF0-12 all stainless electric air heaters (1.2 kW each). An Eagle Model C7180V1 reciprocating single stage compressor [5.4 kW (7.5 hp)] provided the low-pressure (0.2 MPa) air at a rate of 9.1 m^3/min (30 cfm). An Arrow brand model RH203 heatless twin tower regenerative desiccant air dryer (-40° C), with micron particulate filters, was used to ensure that moisture and oil vapor did not accumulate on the pebbles during preheat. The preheat system required two-and-a-half hours to heat the pebble bed from room temperature to 367 K (200°F). The high-pressure air for a tunnel run obtained thermal energy via convection from the pebbles when passing through the pebble bed.

The Mach 5 contoured nozzle was 34.3 cm long with throat area of 1.93 cm^2. A photograph of the nozzle is presented in Fig. 3.3. The nozzle was designed by the PI and constructed in 1995 from a high temperature grade (type 347) stainless steel. The original flow straightner consisted of a single aerogrid (i.e., porous plate) with forty 6.35 mm diameter holes located approximately 3.8 cm upstream of the nozzle contraction. The Mach number was uniform to within 2.0% across the free stream. However, the Mach number in the boundary layer varied significantly in the span wise direction. Because of this variation, a new flow straightner was designed and constructed. The new straightner consisted of two aerogrids each with sixty 3.2 mm holes located 2.54 cm upstream of a new turbulence-dampening screen. Figure 3.4a shows the new flow straightner and the original aerogrid. The new straightner was constructed from a high temperature grade (type RA321) stainless steel. The screen was located approximately 5.1 cm upstream of the nozzle contraction. It is also noteworthy that the stilling-chamber-to-throat contraction area ratio for increased from 13:1 to 19.4:1 with the new straightner. Presented in Figs. 3.4b and c is a comparison of the flow before and after the new flow straightner measured with the Pitot tube in the five-hole-probe. The boundary layer with the new straightner is significantly more uniform across the span of the flow. However, the free stream was only modestly improved.

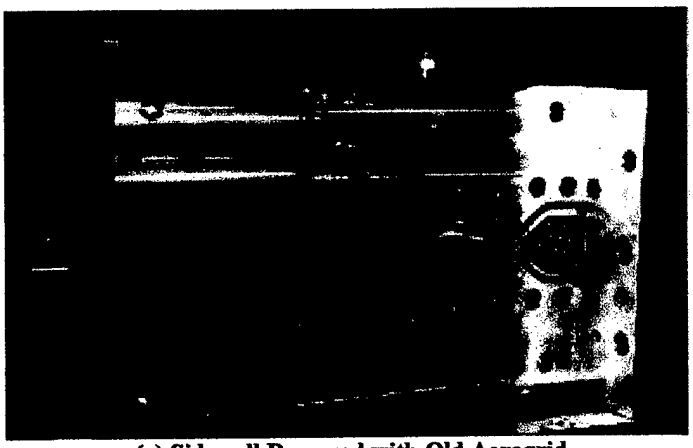

(a) Sidewall Removed with Old Aerogrid

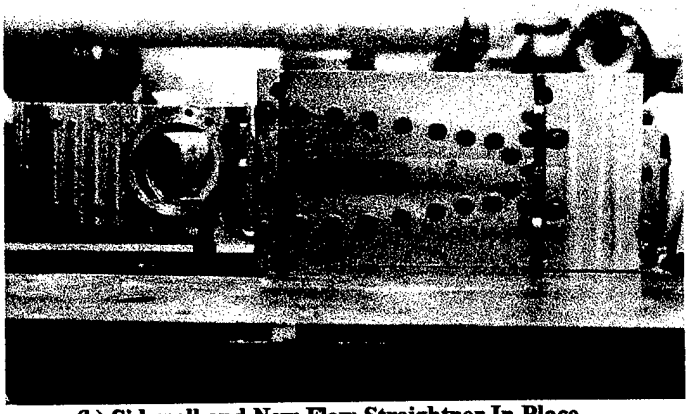

(b) Sidewall and New Flow Straightner In-Place

Fig 3.3 Photographs of the Mach 5.0 Contoured Nozzle

The stilling chamber Pitot pressure was measured with a 0-3.4 MPa gage Endevco Brand Model 8510B-500 piezoresistive pressure transducer with sensitivity 8.44 mvolt/pa. The miniature pressure transducer (3.8 mm face diameter) had a resonance frequency of 500 kHz and stable operation over a temperature range of 0-366 K. It was connected to a 2.38 mm outer diameter stainless tube, which was inserted into the chamber and mounted to the nozzle sidewall by a high-temperature resistant epoxy seal.

The transducer was connected to an Endevco Model 4428A Pressure Indicator with LED pressure display and a 0 - 5volt analog output. An Omega Brand K-type (Chromel-Alumel, 3.15 - 1445 K) thermocouple connected to an Omega Brand Model DP25-TC-A programmable digital thermocouple meter displayed the tunnel chamber total temperature and provided a 0 - 10 volt analog output, with a scale factor of 283.15K/volt. The uncertainties in the total pressure and temperature were ± 0.02 MPa and ± 2 K, respectively.

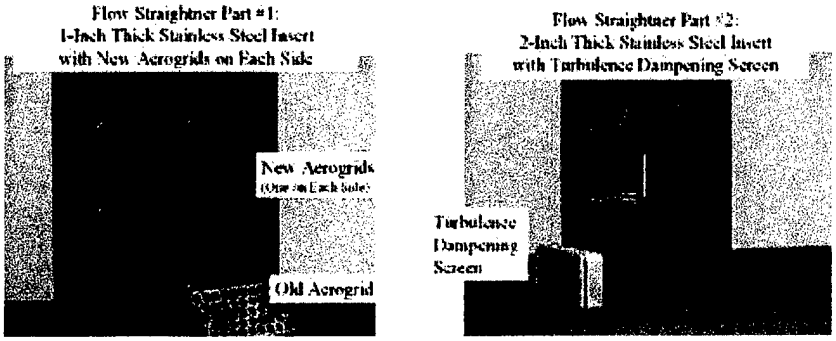

(a) Photographs

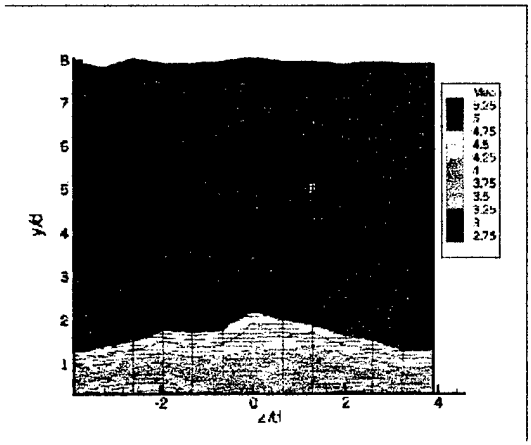

(b) Tunnel Calibration with Old Straightner

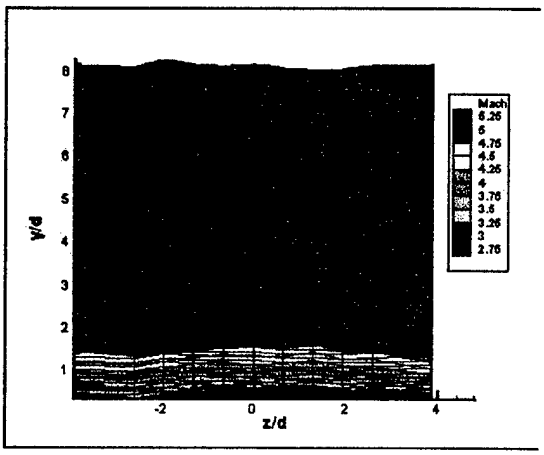

(c) Tunnel Calibration with New Straightner
Figure 3.4 New Flow Straightner

The test section had a 7.62 × 7.62 cm^2 cross-section, with a length of 26.7 cm. The test section sidewalls were constructed from type 347 stainless steel and had optical grade glass windows (flat to within 52 nm/cm) for optical measurements. One of the top walls had three slots with corresponding blocks for probe insertion at different axial positions, and the other was a solid plate manufactured from 4.45 cm thick optical grade Plexiglass for optical access. The wind tunnel models were located in the lower wall. The leading edge of the diamond injectors was located 7.14 cm downstream of the nozzle exit. Shown in Fig. 3.5 is the test section geometry.

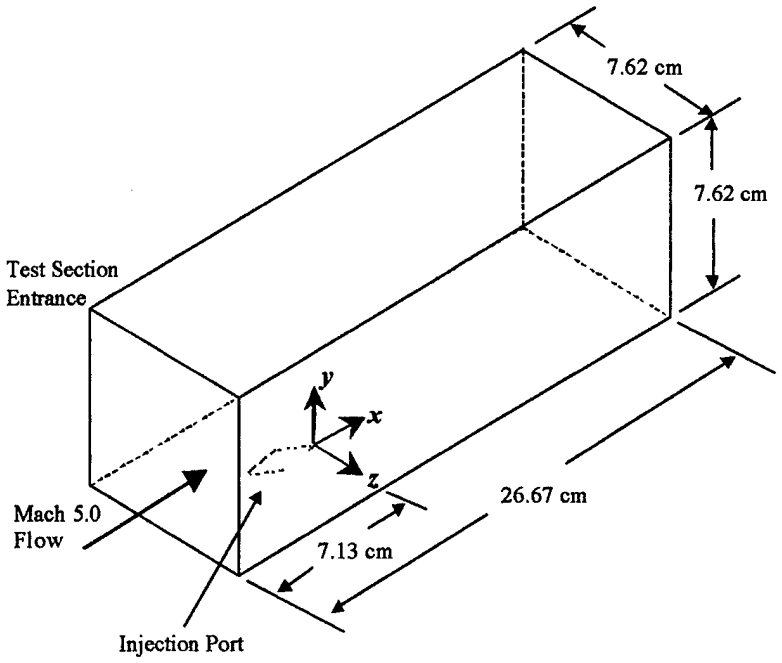

Fig. 3.5 Single-Port Test Section Geometry and Coordinate System

The variable area diffuser was 7.62cm wide and 91 cm long. The throat-area was adjusted to 7.6 cm (28.3 cm downstream of the diffuser inlet), for optimal diffuser efficiency. The minimum pressure ratio was measured at 21, which corresponds to a diffuser efficiency of approximately 75%. Considering the compact size of the diffuser, this efficiency was deemed acceptable. The tunnel air discharged to the atmosphere through an Allied Witan Co. model M60 air sound muffler, which was attached to the diffuser exit through a 15.24 cm (6 inch) pipe.

3.1.3 Low Reynolds Number Calibration Wind Tunnel

The cross-film probes are sensitive to Reynolds number. Hence, the probes had

to be calibrated over the range expected across the injector plumes. Thus, a low Reynolds number calibration in-draft facility was constructed. The facility consisted of a Mach 1.7 contoured nozzle connected to the shock tunnel vacuum receiver tank. The cross-section of the calibration facility was 7.62 x 7.62 cm^2. Shown in Fig. 3.6 is a photograph of the calibration facility. The measured Mach number is 1.73, and the Reynolds number per meter is 14 x 10^6.

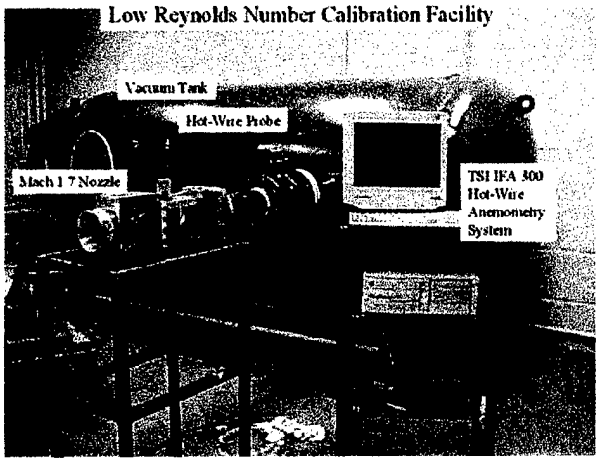

Fig. 3.6 Low Reynolds Number Calibration Facility

3.2 Wind Tunnel Models

3.2.1 Single-port-injectors

Four diamond injectors, with different incidence angles, and one circular injector (90°) were designed, constructed and tested. Figure 3.7 shows the injector schematics. The effective diameter of all injectors was 4.89 mm. The ducts for the diamond-shaped injectors were machined to angles of 10°, 27.5°, 45°, and 90° respectively with respect to the surface of the injector exit port. A 135° injection was achieved by operating the 45°

injector backwards. All of the single port diamond injectors had a 15° vertex half angle. This small angle was chosen to ensure attached shock waves near the wall and to minimize the effects by the reflected waves from the side-walls. The injector was mounted on the bottom plate of the test section as shown in Figure 3.5. The injectant air was induced into the wind tunnel model through an aluminum duct with a diameter of 1.27 cm. The jet exit Mach number was 1.0. The jet-to-free stream momentum flux ratio (J) was varied by varying the injector total pressure. The jet flow conditions are listed in Table 3.2.

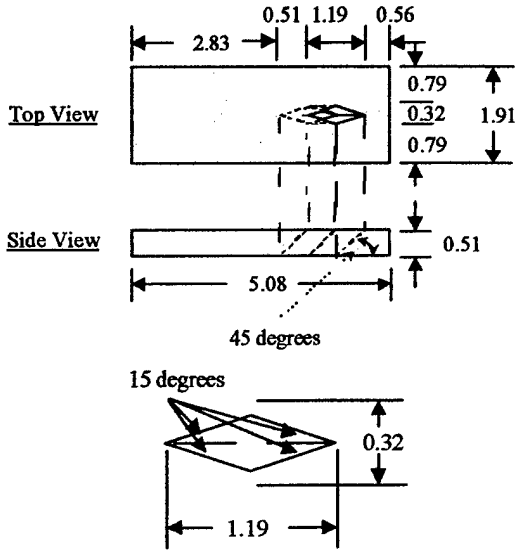

Fig. 3.8 Schematic of the Single Port Injector (45° Injector Shown)

Table 3.2 Test Matrix

Test Condition	*Injector geometry*[a]	α[b] *(deg)*	C_D[c]	J[d]	J_{eff}[e]	p_t *(MPa)*	p_j/p_∞[f]
1	SD	10.0	0.23	0.43	0.08	0.10	8.4
2	SD	27.5	0.41	0.43	0.16	0.10	9.7
3	SD	45.0	0.67	0.43	0.27	0.10	10.0
4	SD	90.0	0.94	0.43	0.40	0.10	10.3
5	SC	90.0	0.99	0.43	0.42	0.10	10.3
6	SD	135.0	0.67	0.43	0.27	0.10	10.0
7	SDTR	45.0	0.67	0.43	0.27	0.10	10.0
8	SDDR	45.0	0.67	0.43	0.27	0.10	10.0
9	SD	10.0	0.24	1.91	0.41	0.10	41.1
10	SD	27.5	0.41	1.91	0.76	0.45	45.5
11	SD	45.0	0.68	1.91	1.29	0.45	46.4
12	SD	90.0	0.91	1.91	1.74	0.45	46.7
13	SC	90.0	0.90	1.91	1.72	0.45	47.3
14	SD	135.0	0.68	1.91	1.29	0.45	46.4
15	SD	10.0	0.15	2.59	0.33	0.59	54.6
16	SD	27.5	0.42	2.59	1.03	0.59	60.5
17	SC	45.0	0.67	2.59	1.68	0.59	61.7
18	SD	90.0	0.95	2.59	2.40	0.59	62.1
19	SC	135.0	0.67	2.59	1.68	0.59	61.7
20	SDTR	45.0	0.67	2.59	1.68	0.59	61.7
21	SDDR	45.0	0.67	2.59	1.68	0.59	61.7

[a]SD: single port diamond, SC: single circular, SDTR: single port diamond with tapered ramp, SDDR: single port diamond with double ramp.[b]Injector incidence angle. [d]J = ideal momentum ratio. [e]J_a = effective momentum ratio accounting for viscous losses [see Bowersox et al (2003)]. [f]Effective pressure ratio, $Tj/T_\infty = 4.0$ and $u/u_\infty = 0.41$.

The tapered ramp of Wilson, Bowersox and Glawe (1998) was chosen to enhance the plume vorticity, where in the Wilson et al. study, this ramp produced the largest gain in plume vorticity. The 45° diamond injector was chosen as the test bed for the variable wall geometry ramp. This ramp was designed such that the ramp angle matched that of the injector (45°) and the height was chosen so that the vertex of the ramp was adjacent to the lower side of the plume. These measures were taken to ensure strong ramp-plume interaction, while not overwhelmingly distorting the flow with the ramp. Figure 3.8

shows the final ramp geometry.

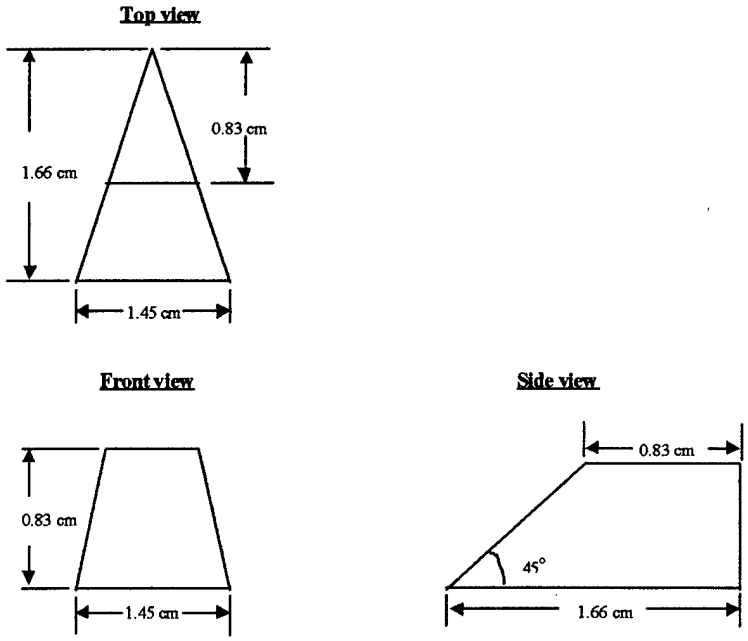

Fig. 3.9 Schematic of Variable Wall Tapered Ramp [Design Based on Wilson, Bowersox and Glawe (1998)].

3.3 Computational Facilities

The bulk of the numerical simulations were performed on the Air Force ASC HPC Compaq and Origin computer systems.

3.4 Instrumentation

3.4.1 Surface Oil Flow Visualization

Dow Corning Brand 200 fluid (Dimethicon) with a kinematic viscosity of 1000

centistokes, which is a medium viscosity linear polydimethylsiloxane polymer, was used for surface oil flow visualization. Day-Glo Color T-15 blaze orange fluorescent pigment was mixed with the fluid. The mixture was spread on the bottom surface of the test section and illuminated by an ultraviolet lamp through the top surface of the wind tunnel, which was constructed from optical grade Plexiglass. Photographs of the oil patterns were taken with a Kodak Professional DCS 460c color digital camera that was mounted on a tripod above the top plate. The Kodak camera back, which was attached to a Nikon N90 camera body, had a high-resolution 3060x2036 pixel color Charge Coupled Device (CCD) imager. A Nikon N90 50 mm lens was used, and the shutter speed and fstop were 1.3 and 2.8, respectively. The camera was connected by a SCSI port and cable to a NEC personal computer with a 300 MHz Intel Pentium 2 processor, 64MB Sync DRAM, 8.4GB hard drive PC that operated with Microsoft Windows 98. On the computer, an Adaptec AVA-1502 SCSI Host Adapter with a SCSI2 port transferred the digital images recorded by CCD imager to the computer, where the images were acquired and displayed through the Kodak TWAIN driver into the Adobe Photoshop 4.0 application software for Windows. The image recording was controlled via the Adobe Photoshop program.

3.4.2 Two-Color Digital Particle Image Velocimetry (PIV)

The laser sources used for the present PIV measurements were two Continuum Brand Surelite SL I-10 Nd: NAG laser systems. The two Surelite Nd:NAG lasers each produced coherent green (532 nm) laser beams. The red (607 nm) laser beam was formed by passing one green beam through a SulfaRhodamine (640 nm) methyl alcohol

solution dye laser. The two (green and red) laser beams were then merged in space through a dichroic splitter, and the resulting co-located beams were passed through sheet-forming optics and directed into the test section. The temporal delay between the red and green laser was set at 200 ns with a Stanford Research Systems Model DG535 four-channel digital delay/pulse generator. The Kodak Model DCS 460 high resolution CCD camera (described in the previous Section) with Nikon N90 50mm and 150 mm lenses were used to record the Mie scattering color images.

A TSI Brand Model 9306 Six-Jet Atomizer was used to produce olive oil seed particles with mean aerodynamic diameter $\leq 0.6\mu m$. The particles were injected with the injector air. Because of the high pressures associated with the Mach 5.0 wind tunnel, the seed generator was placed inside a pressure vessel.

Because of the high fidelity temporal laser separation control, the digital two-color system was well suited for hypersonic flow. The PIV system provided direct measurements of the instantaneous planar velocity (in the x and y directions) and vorticity. In addition, the instantaneous Mie scatter images provided qualitative insight into the large-scale turbulent structure of the flow. Unfortunately, this PIV system was not robust enough to acquire enough images for statistical turbulence measurements. More specifically, the camera acquisition rate translated into one PIV image per tunnel run. Hence, only instantaneous information was obtained.

3.4.3 Mie Scattering Flow Visualization

Two types of Mie scattering flow visualization images were acquired,

instantaneous and time averaged. For the instantaneous images, two pulsed Continuum brand Surelite Nd:YAG were used. The pulse duration was 10 ns and the repetition rate was 10 Hz. The lasers produced two coherent green (532 nm) beams. One beam was used to pump a dye [SulfaRhodamine (640nm) methyl alcohol solution] laser to generate a red (640 nm) beam. The two (green and red) laser beams were merged in space with a dichroic splitter, and the resulting co-located beams were passed through sheet-forming optics and directed into the test section through an optical grade Plexiglas ceiling. The temporal delay between the red and green laser was set at 200 ns with a Stanford Research Systems Model DG535 four-channel digital delay/pulse generator. The two-color system allowed for instantaneous velocity measurement.15 A TSI Brand Model 9306 six-jet atomizer was used to seed the injectant with olive oil particles. The 3dB frequency response of for this 0.5- 1.0 mircometer diameter seed material has been previously established at 60 – 220 kHz.19 The scattered light from both the red and green laser pulses was collected with the CCD camera described in the previous section. For the time averaged Mie scattering images, only one laser was used and the camera exposure was increased so that 30 laser pulses were captured on a single CCD image.

3.4.4 Pressure Sensitive Paint (PSP)

Pressure sensitive paint (PSP) provides surface pressure distributions with larger areas and finer spatial resolution than conventional pressure ports. The ISS, Inc. Brand platinum octaethylporphyrin (PtOEP) pressure sensitive paint was used to measure the surface pressure distribution around the jet port. It had absorption maxima at excitation

wavelengths of 380 and 540 nm, with an emission at 650 nm. Because the present pressure sensitive paint utilized fluorescence, a relatively high frequency response (~ 1 msec) was achieved. The intensity of the imaged surface is governed by the Stern-Volmer relation (i.e., $I_o/I = 1 + cp/p_o$), where c is constant that depends on the molecular properties of the paint. The actual calibration was slightly more general (i.e., $I_o/I = a + bp/p_o$).

The paint, when excited with a blue LED light source, produced photoluminescence in order to lose the absorbed energy, and some of the photoluminescence was quenched by the local oxygen (a pressure dependent parameter). Hence, the luminescence intensity was pressure dependent. The luminescence intensity generated by the coating was then collected by the Pixelvision SpectraVideo Brand CCD back-illuminated gray-scale camera, model SV512V1A/PFT-95 with a Nikon f/16-50 mm lens. Uncertainty estimates are listed in Table 3.1.

3.4.5 Traverse and Linear Voltage Displacement Transducer

The traverse system consisted of a 15W Bodine Electric Model NSH-12 DC fractional horsepower gear motor that drove a slide, which moved the probe up and down in the *y*-direction. The traverse speed was controlled by a Minarik Electric Model SL15 controller. The speed was set as 7.62 mm/s (at 70% of full power). The start and stop of the traverse was controlled by a Magnecraft Electric W211ACPSOX-5 delay on start relay and a Magnecraft Electric W211ACPSRX-5 delay on ending relay, respectively. To obtain measurements during the steady flow period, the traverse system was delayed two

seconds after the tunnel start, and stopped to end traverse measurement after five seconds.

The position of the probe was recorded by an Omega Model LD100-150 Linear Voltage Displacement Transducer (LVDT) with nominal linear range 152.4 mm. The LVDT is a precision variable inductor with frequency response up to 15 kHz. An Omega Model SP200A signal processor received signals from LVDT, and generated a DC voltage proportional to the inductance, which was linear with core displacement. The uncertainty of LVDT measurement was 0.067 mm.

3.4.6 Five-Hole Pressure Probe

An Aeroprobe Inc. Brand five-hole-probe was used to measure the local mean Mach number, Pitot pressure, static pressure and total pressure. The probe was a 19° semi vertex angle axisymmetric cone constructed from stainless steel, with a blunted tip containing the Pitot probe. There were four elliptical shaped pressure taps, formed from 0.79 mm outer diameter tube, at a 90° interval around the circumference of the cone. The cone tip was soldiered to an L-shaped 1.59mm outer diameter stainless tube, which held five 0.79 mm outer diameter miniature stainless tubes. The space between the tubes was filled with steel wire and epoxy to prevent displacement. The L shape tube was inserted into a 6.35mm thick and 14.6cm long stainless streamlined strut with sharp leading and trailing edges. The five taps, which were connected to the five 0.79 mm outer diameter miniature stainless tubes, were connected to the pressure transducers through five 1.59 mm outer diameter miniature Tygon R-3603 tubes. The Pitot pressure was measured an

Omega 0-0.69 MPa (0-100 psia) Px139-100A4V pressure transducer, and the four static pressures were measured with four Omega 0-0.10 MPa (0-15 psia) Px139-15A4V transducers. All five transducers were excited with an Omega PSS-5A power supply. Each transducer had an output 0.25-4.25volts and a 4.8mm outer diameter inlet connector. Based on the normal shock and Taylor-MacColl conical flow theory, the Mach number is a unique function of the ratio of the cone-static and Pitot pressures. The numerical conical flow and Rayleigh Pitot solution is tabulated Table 3.2. A curve fit for the Mach number as a function of the pressure ratio is given by

$$\frac{1}{M} = -1.424 + 24.873\left(\frac{P_c}{P_{t2}}\right) - 158.089\left(\frac{P_c}{P_{t2}}\right)^2 + 566.284\left(\frac{P_c}{P_{t2}}\right)^3$$
$$-1124.770\left(\frac{P_c}{P_{t2}}\right)^4 + 1165.510\left(\frac{P_c}{P_{t2}}\right)^5 - 491.796\left(\frac{P_c}{P_{t2}}\right)^6$$

The percentage differences between the curve fit and the exact theory are also listed in Table 3.2. A comparison of the calibration curve fit to the numerical solution is given in Fig. 3.11. The remaining flow properties were computed using the usual compressible flow relationships [Anderson (1990)]. An important inference from Fig. 3.11 is that at high Mach numbers, greater than 5.0, the change in Mach number becomes very sensitive to small changes in the pressure ratio; this is because of hypersonic similarity. Hence, the uncertainties in the Mach number are amplified at higher Mach numbers. The uncertainty estimates for the Mach number and static pressure acquired with this probe listed in Table 3.1 are given as a function of Mach number. It is also noteworthy that the

present study was focused on the plume and boundary layer regions of the flow ($M < 5$), and thus, the hypersonic similarity difficulty was avoided.

3.4.7 Shadowgraph

The optical system for the shadowgraph consisted of a mercury vapor light source and a mirror to form a parallel column of light. The beam was passed through the test section and onto a reflective screen to form the shadowgraph image. The shadowgraph images were digitized with the Kodak CCD camera mentioned above.

3.4.8 Data Acquisition Boards and Testpoint Software

The analog signals from the various probes (except the cross-film, discussed in the next paragraph) were converted to digital signals with a 12-bit resolution, Keithley Model DAS-1802AO low-gain data acquisition board. This system could acquire data at a rate up to 333 ksamples/s, with a maximum A/D throughput of 312.5 ksamples/s for operation in the 0-5volt unipolar mode. All channel inputs were within a range of 0-5 volt in order to increase total system throughput and reduce noise by using the same gain for all channels. The system is software-configurable for sixteen single-ended onboard channels or eight differential channels. The data board, with the STA-1800U screw terminal I/O interface accessory, was connected to an IBM Pentium(r) OverDrive 56MB RAM PC operating Windows 98. The Capital Equipment, Inc. data acquisition control software package Testpoint was used to control the data acquisition. The total number of samples and sampling frequency were 10,000 and 1 kHz, respectively. Consequently, the

data-taking period was 10 seconds.

3.5 Flow Solver, Numerical Domain and Solution Methodology

GASP (Aerosoft, Inc.) is a commercial finite-volume, structured, multi-block, compressible code with the ability to solve both unsteady and steady RANS equations. In addition, GASP can also solve the parabolized Navier-Stokes, the Euler equations, and the incompressible Navier-Stokes equations. Time accurate solutions can also be obtained through an implicit or explicit procedure.

Turbulence can be modeled in GASP using a variety of equations. The set of equations include the algebraic model of Baldwin-Lomax, the one-equation model of Spalart-Allmaras, and two-equation models such as $k-\varepsilon$ and $k-\omega$. Inviscid fluxes can be chosen from the standard Roe, Van Leer, Roe with Harten's correction, preconditioned Roe flux, AUSM+, full flux for solving parabolized Navier-Stokes, and the artificial compressibility method for solving incompressible flows.

GASP version 4.0 includes new features such as the ability to model complex geometries using Chimera/overset grids. The code can be executed on shared and distributed memory machines. This is accomplished by using the message passing interface (MPI) libraries.

Initial simulations of the flow were performed on a Cartesian grid in which the injector was modeled using a stair case arrangement of cells along the tunnel wall. A constant velocity profile was specified as the boundary condition for the injector. This was found to be inadequate since losses in the injector port were neglected and also the

penetration was found to be higher. Availability of GASP version 4.0 along with the construction of a twenty four-node Beowulf class computer made it feasible to increase the grid size to obtain better resolution of the flow. Also the injector port was modeled to include the injector port losses.

Figure 3.10 shows the current grid used in the simulations. The grid is composed of six blocks with a total of 5.26 x 10^6 cells. Grid dimensions are listed in Table 3.3. Only a quarter of the physical domain was modeled since the flow is symmetric about the centerline of the tunnel and the region of interest was below a height of $y/d = 8.0$. Grid lines are clustered near the tunnel floor to satisfy $y^+ < 1$. Grid lines are also clustered close to the injector exit to capture important flow features. The grid lines normal to the tunnel floor are aligned in the shock direction within the limits of the desired grid quality.

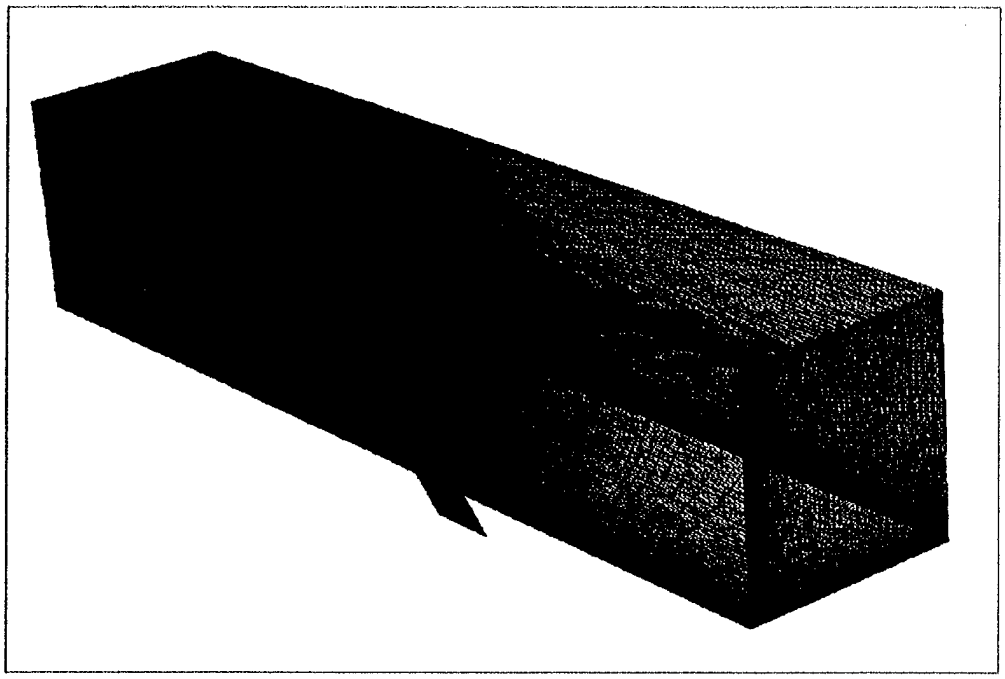

Figure 3.10 Computational Grid

Table 3.3 Grid Dimensions

Block	Fine Grid	Medium Grid	Coarse Grid
1	21 x 151 x 101	11 x 76 x 51	6 x 26 x 26
2	281 x 151 x 101	141 x 76 x 51	141 x 26 x 26
3	81 x 151 x 41	41 x 76 x 21	41 x 26 x 11
4	21 x 151 x 31	11 x 76 x 16	11 x 26 x 16
5	81 x 51 x 41	41 x 26 x 21	41 x 26 x 11
6	21 x 51 x 31	11 x 26 x 16	11 x 26 x 16
Total Cells	5260000	657500	118125

Inlet conditions for the tunnel were obtained from a flat-plate calculation to match experimental boundary layer thickness δ. Adiabatic wall conditions were used for the tunnel floor and the injector wall. Symmetry conditions were used for the plane along the centerline of the tunnel. Density and pressure were used for the injector inlet conditions.

Slip boundary conditions were used for the outer wall of the tunnel. All other boundaries were extrapolated. Figure 3.11 shows the computational domain with associated boundary conditions.

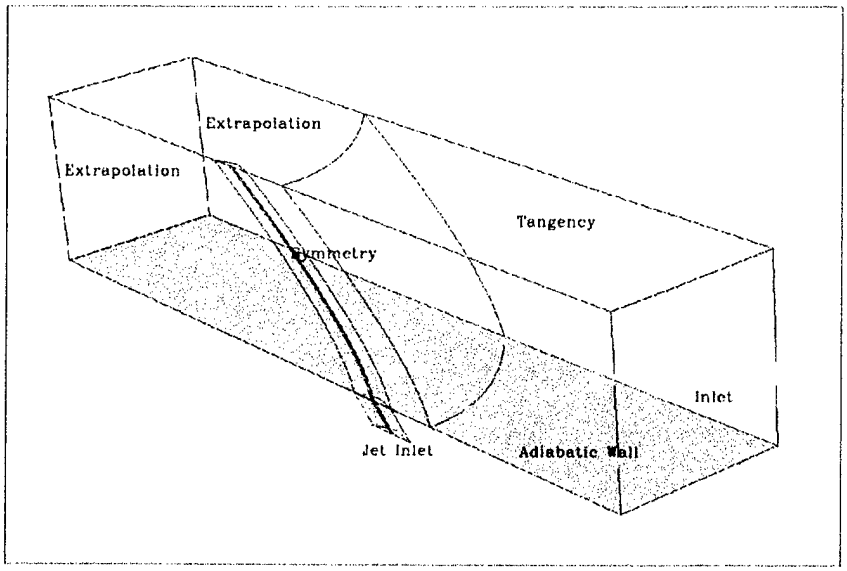

Figure 3.11. Boundary Conditions.

The $k-\omega$ [Wilcox (2000)) turbulence model with compressibility correction was used in this simulation. Roe flux [Roe (1981)] along with the min-mod [Hirsch (1992)] limiter and a third-order upwind scheme was used for the inviscid flux. Laminar transport properties were modeled using the Sutherland viscosity and conductivity models and the constant Schmidt number Diffusivity model. A turbulent Prandtl number of 0.9 and turbulent Schmidt number of 0.5 were used. Gauss-Seidel technique along with Gauss-Seidel inner iterations was used to obtain the solution for all global iterations.

Both grid and solution convergence were based on the centerline floor pressures. Grid convergence was performed in situ using the grid sequencing technique available in

GASP. The number of cells in each grid level is listed in Table 3.3. The centerline pressures for the three grid levels are given in Fig. 3.12. Solution convergence was monitored by plotting the centerline pressures every 25 iterations. The solution was deemed converged when the change in the centerline pressure was negligible. Figure 3.12 shows a representative plot of the centerline pressure for the 90°, 0.1 MPa jet total pressure.

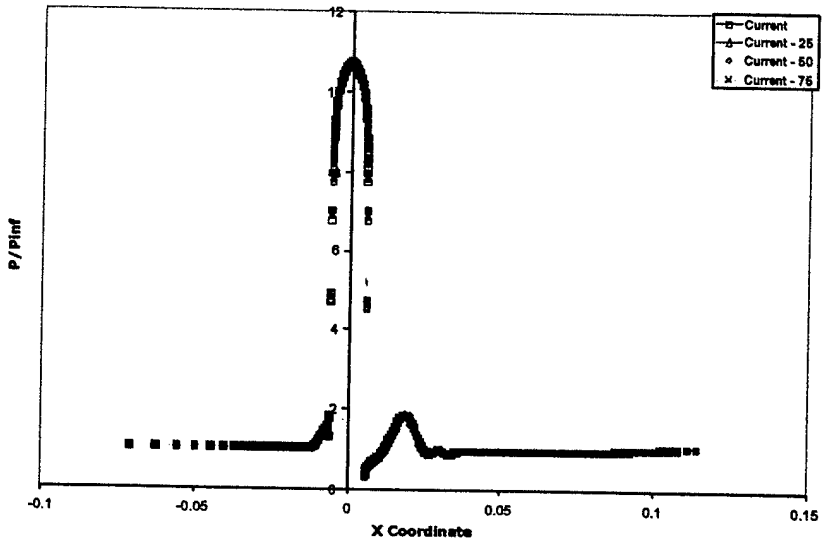

Figure 3.12 Solution Convergence Plot

Chapter 4

Results and Discussion

4.1 Experimental Results and Discussion

Surface Oil Flow Visualization

Surface oil flow visualizations were acquired for all of the no-ramp conditions listed in Table 3.2. The results are shown in Fig. 4.1. The diamond injector results were divided into two basic categories: attached and detached leading edge shocks. Representative examples of each diamond injector type are shown in Figs. 4.2a and 4.2b, where the freestream is from left to right, and the jet flow is directed outward from the paper. Shown in Fig. 4.2c is the high-pressure circular injector result. Examining the attached case given in Fig. 4.2a (low-pressure, $\alpha = 27.5°$), the first flow feature, moving from left to right is a curved line of oil accumulation enclosing the diamond-shaped injector exit. This line is attached to the injector leading edge, and is essentially co-located with the jet interaction shock in the region near the injector; this is confirmed with the pressure sensitive paint measurements described below in the Pressure Sensitive Paint section. However, further downstream, the shock wave strength decreased and approached a Mach wave, and hence it was no longer coincident with the line of separation. The second curved line of oil accumulation that wrapped around the jet indicates the location of a small horseshoe vortex. Third, two wake vortex lines due to up-wash[10] were observed to emanate at the injector trailing edge. Fourth, between the wake vortex lines is the reattachment line. In general, the flow topologies for the

detached shock cases (e.g., Fig. 4.2b) were similar to those of the attached shock case. The obvious exceptions are (1) the detached leading edge jet interaction shock and (2) the horseshoe vortex was more pronounced and it reached further upstream for the detached shock case. The circular injector flow topology (Fig. 4.2c) was very similar to the detached diamond injector (Fig. 4.2b). However, when compared to the detached diamond injector flow, the circular injector shock standoff distance was larger and the angle between the wake vortex lines was lower. In general, the topology described above is very similar to the lower Mach number results of Tomioka et al.[16]

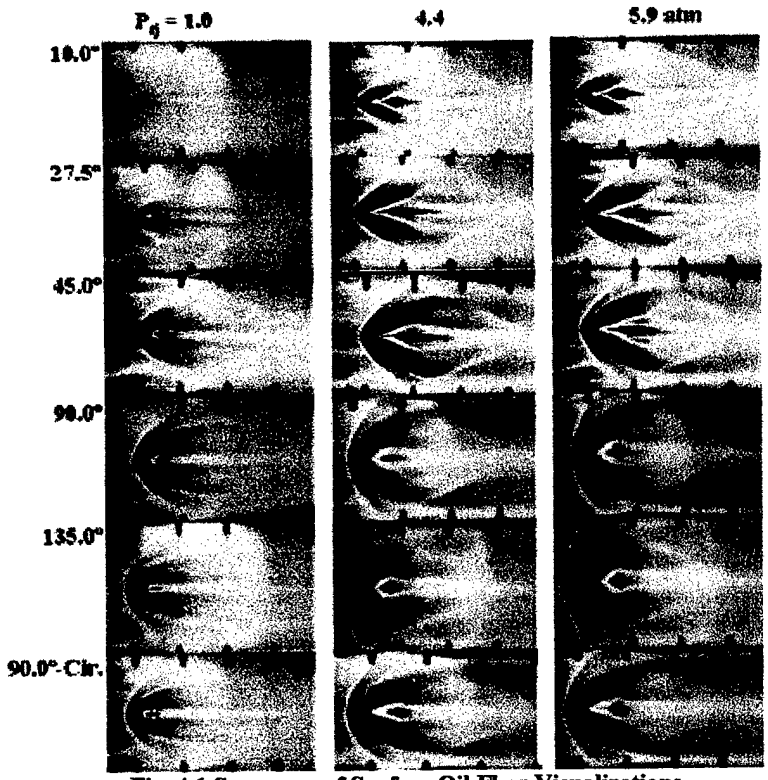

Fig. 4.1 Summary of Surface Oil Flow Visualizations

(a) Low-Pressure, $\alpha = 27.5°$

(b) High-Pressure, $\alpha = 90°$

(c) High-Pressure, $\alpha = 90°$

Fig. 4.2 Representative Surface Oil Flow Visualizations

Upon examination of the surface oil flow visualizations for all of the injection angles (10 - 90°) at both injection pressures, the following specific observations were drawn. First, the state of the leading edge shock wave (attached or detached) for the diamond injectors depended on both α and the injector pressure. The shocks were attached for the low-pressure, $\alpha = 10°$ and 27.5° cases. The shock standoff distance was

very small for the 45° case. As α increased from 10° to 45°, the leading edge shock angle increased from 35° to 52°. The increase is explained by recognizing that the discharge coefficient, and hence mass flux, increased significantly with injector angle (see Table 3.2). Moreover, as α increased, the 3-D relieving effect[20] decreased.

Focusing now on the medium-pressure results, the shocks were attached for α = 10°. For α = 10° to 45°, the shock angles were nominally 10° larger than the corresponding low-pressure cases. Also, compared to the low-pressure data, the high-pressure wake regions were wider in the z-direction; the wakes and wake vortices extended further downstream, and the horseshoe vortices reached further upstream. For the detached shock cases, the high-pressure shock strength was larger than the corresponding low-pressure results, as indicated by the larger lateral extent of the nearly normal shock region and the larger shock wave detachment distance. The explanation for all of these observations is that the higher-pressure jets expanded more when injected into the freestream creating additional blockage and penetration, and thus the above listed observations. Similar observations hold for the highest pressure.

Shadowgraph Photography

Shadowgraph images were acquired for all of the no-ramp conditions listed in Table 3.2. The results are summarized in Fig. 4.3. In these figures, the cross flow is from left to right, and the injector port is in the tunnel floor. The present discussion will focus on the three cases described above. First, the attached shock case corresponds to the low-pressure, α = 27.5° test condition. A clearly defined jet interaction shock is depicted, and

the barrel shocks are faintly visible. When compared to the medium pressure, $\alpha = 90^{\circ}$ case, the main difference between the detached and attached shock shadowgraphs is the presence of the lambda shock, which was created by the stronger detached bow shock wave interaction with the tunnel boundary layer. The shock structure for the circular injector was similar to that for the detached injector.

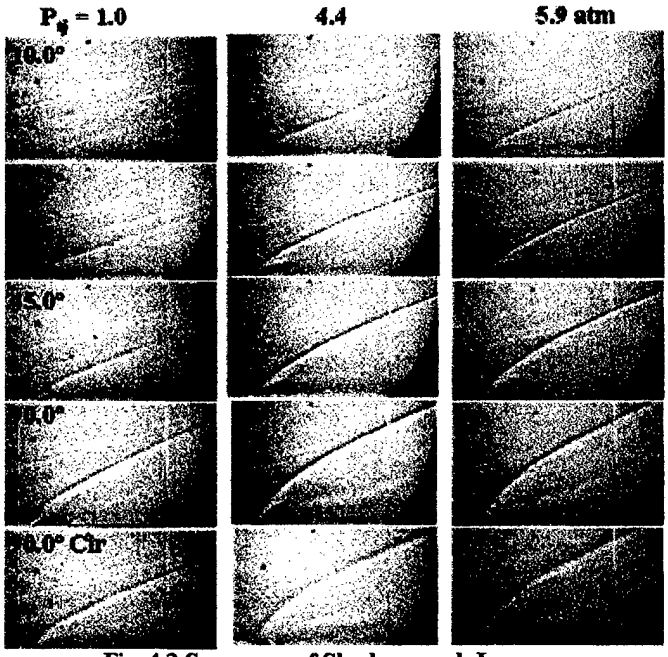

Fig. 4.3 Summary of Shadowgraph Images

Examination of all of the shadowgraphs confirmed the trends described above. Specifically for the low-pressure, $\alpha = 10^{\circ}$ and 27.5° cases, leading edge lambda shocks were not present indicating an absence of upstream flow separation. For $\alpha = 10^{\circ}$ to 45°, the shock angles increased from 30° to 49° with jet incidence angle, demonstrating that the shock strength, and hence total pressure loss, increased with jet incidence angle. Quantification of the shock losses is described in the later. The 90° diamond and 90°

circular cases both had lambda shocks, indicating flow separation. Barrel shocks were visible for the 45° - 90° cases. However, they were not visible for the remaining two lower angle cases. It was expected that for the lower angles, the barrel shocks were not as strong due to the lower discharge coefficients, and subsequent reduced pressure (listed in Table 3.2). In addition, the jets did not penetrate very far into the freestream; hence, the barrel shocks were blurred by the tunnel boundary layer. The initial shock angles for each incidence angle were noticeably larger (8° - 13°) for the high-pressure conditions as compared to the corresponding low-pressure cases. Lambda shocks were present for all but the lowest angle case, and the barrel shocks were clearly visible in all of the high-pressure shadowgraphs.

Mie Scattering Imagery

Summarized in Fig. 4.4 are the mean Mie-scattering flow visualizations. Compared in Figs. 4.5a and b are the instantaneous images for the low-pressure, $\alpha = 27.5$ and 90° cases. In both images, the freestream flow is from left to right. The instantaneous image shows that large-scale turbulent structures were present in the jet plumes; however, the size of the structures near the jet orifice appeared to have increased with increasing incidence. For the 90° case shown in Fig. 4.5b, the tunnel was intentionally run approximately 5.0K below the oxygen liquefaction temperature to produce Rayleigh scattering from the condensed liquid oxygen in the freestream. Hence, the tunnel boundary layer, just upstream of the injector port and the jet interaction shockweare visible due to vaporization of the oxygen in the warmer boundary layer and across the

shock. This rather unique flow visualization indicated that even though the jet interaction shock for this case was detached near the wall (Table 2), it re-attached to the jet near the point where the plume bent over towards the freestream direction. In addition, the jet plume narrowed in this region, which is indicative of the plume spreading more in the lateral direction;[13] Fig. 5a shows a similar phenomenon.

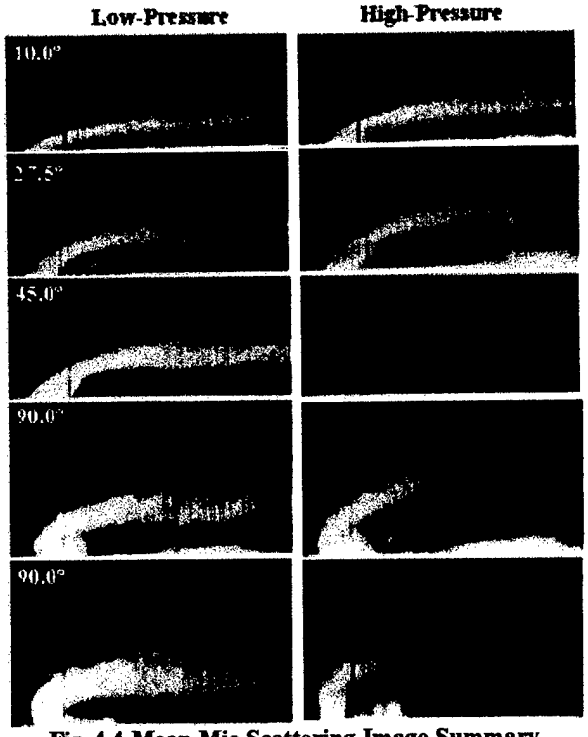

Fig. 4.4 Mean Mie Scattering Image Summary

The time-averaged data (examples are shown in Figs. 4.5c-e) show more clearly, the upper edge and hence mean penetration of the plume into the freestream. Time averaged Mie scattering images were obtained for the first two pressure cases listed in Table 3.2. It was also apparent that the plume narrowing described in the previous paragraph was present for all of the diamond injectors, and absent for the circular injector. Visual

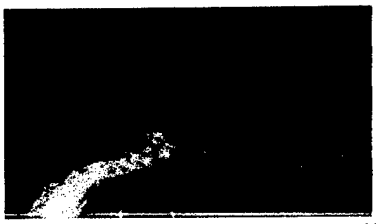

(a) Upper: Low-Pressure, $\alpha = 45°$

(b) Lower: Low-Pressure, $\alpha = 90°$

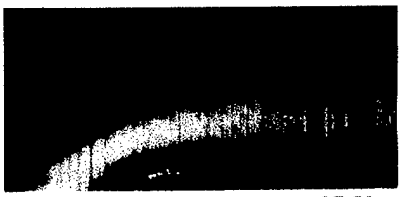

(c) Low-Pressure, $\alpha = 27.5°$

(d) High-Pressure, $\alpha = 90°$

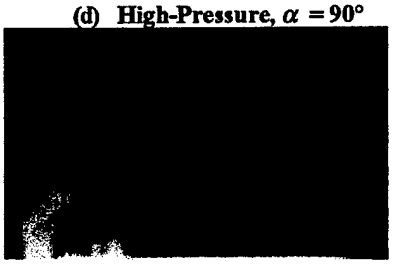

(e) High-Pressure, $\alpha = 90°$

Fig. 4.5 Representative Mie-Scattering Flow Visualizations

measurements of the centerline penetration (y_p/d) were obtained from these data for x/d less than about 8.0. The jagged plume edges seen in Fig. 4.5 resulted in scatter in the y_p/d measurements ranging from about ±0.1, close to the jet exits, to approximately ±0.2 at the downstream limit of the measurement ($x/d \approx 8.0$).

Various power-law correlation methods have been proposed for penetration.[8,13] A generalized form for these correlations for the present sonic injection into a Mach 5.0 freestream was written as $y_p/d = f_p(\xi)$, where $\xi = J_{eff}^m(x/d)^n$. For the present study, $J_{eff} = J\sin\alpha$, and the values of J are listed in Table 2. Plotted in Fig. 4.6 are all of the penetration data with the above scaling. As indicated in the plot, the diamond and circular injector data collapse reasonably well (variation in y_p/d is within the scatter of the data) onto to two separate curves, one for the diamond injectors and the other for the circular injectors. For both data sets, n was found to be nominally 0.33; this value is consistent with previous studies at lower supersonic freestream Mach numbers.[13] Values of 0.15 and 0.26 for m were found to collapse the diamond and circular port data, respectively. The function $f_p(\xi)$ for the circular injector data was the straight line $y_p/d = 1.93\xi + 0.40$, where the linear form agrees with previous studies.[13] The nonzero intercept reflects the fact that the plume expanded upstream of the injector port (see Fig. 4.5d). For the diamond injector, $f_p(\xi)$ was linear to within the experimental scatter for ξ greater than about 1.0, with a slope of 2.65. However, for ξ less than 1.0, the data systematically dipped below the linear trend. A hyperbolic curve was incorporated to fit the data over the full range of ξ shown in Fig. 6; the resulting equation was $y_p/d = [1+(2.65\xi)^2]^{1/2}-1$. The reproduction of the penetration was within the expected uncertainty of the data.

Penetration measurements at x/d = 7.5 are listed in Table 2 (column 8) for all of the test conditions. From these data, the following specific conclusions were drawn. First, for the diamond injectors, the penetration at x/d = 7.5 increased by 70 and 90% as α increased from 10 to 90°, for the low- and high-pressure cases, respectively. Second, for given incidence, the penetration increased by nominally 30% going from low to high pressure for all of the diamond injectors; for the circular injector, the increase was 50%. Also, comparing the 90° diamond and circular injectors, the magnitude of the penetration was essentially the same at x/d = 7.5. The data and correlations shown in Fig. 4.6 also show that the penetration for the circular injectors at both pressures exceeded that of the 90° diamond injectors, for x/d < 7.5. However, the plume trajectories, i.e., slopes, for the 90° diamond injectors were approximately 30% larger than those for the circular port at x/d = 7.5. Hence, it is anticipated that the downstream penetration for the 90° diamond injectors would exceed that of the circular injectors, which agrees with a previous study.[16]

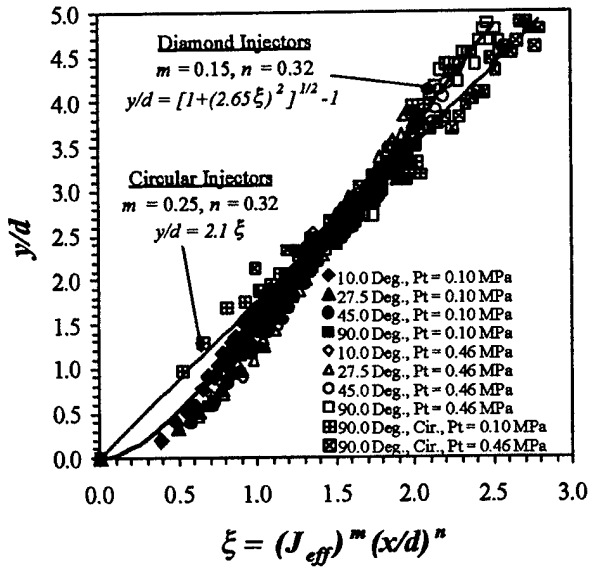

Fig. 4.6 Penetration Correlation Results

Mach Number Contour Data

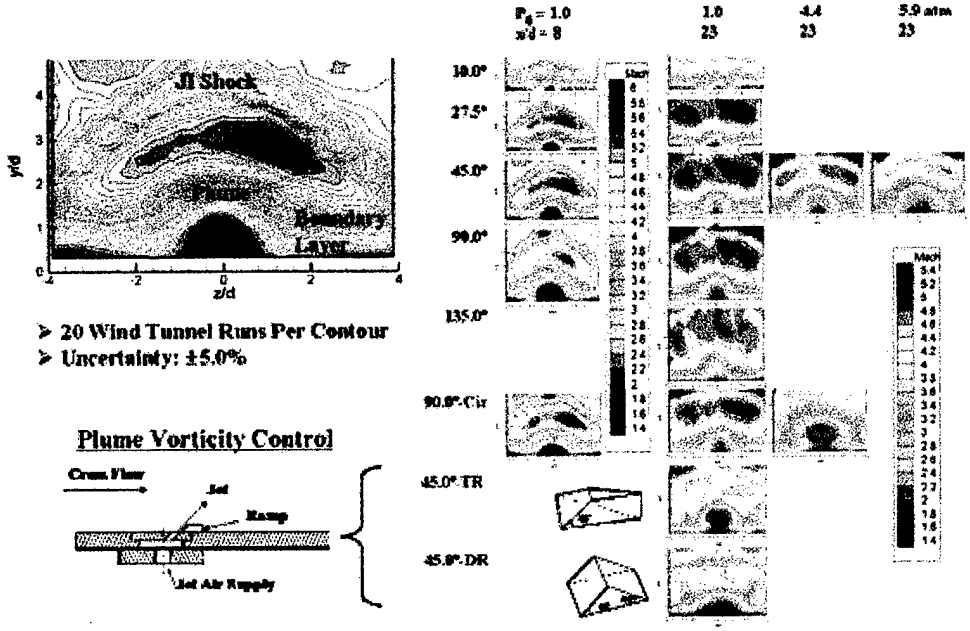

Fig. 4.7 Mach number Contour Summary

The Mach number contours are shown in Fig. 4.7. Examining the Mach number contour for the low-pressure, $\alpha = 45^{\circ}$ diamond shaped injector first (enlarged contour on the left). Starting at the top, the interaction shock wave is the roughly diamond shaped structure with the vertex located at $z/d \approx 0.0$, $y/d \approx 4.2$, and that arched down to $z/d \approx \pm 3.9$ at $y/d \approx 2.0$. The narrow high-Mach region below the shock is the inviscid shock layer between the shock and the plume. The lower extent of the shock layer corresponds to the upper boundary of the plume, which at the centerline ($z/d = 0.0$) was located at $y/d \approx 2.8$-3.2. Now focusing on the bottom of the contour, the wake or up-wash[10] region, is seen as the low Mach, semicircular region centered at $z/d = 0.0$. The vertical extent of this region ($y/d \approx 1.4$) coincides with lower "edge" of the plume as inferred from the Mie scattering images. The tunnel boundary layers are also noticeable on both sides of the contour. The boundary layer thinning in the areas adjacent to the wake resulted from entrainment of low momentum boundary layer fluid into the plume and wake.[11] Above the wake region is the plume. Although the plume edges are not discernable in Fig. 4.7, the expected kidney bean[6] shape of the plume can be inferred from the Mach contours. Specifically, starting at the midpoint of the lower edge of the plume ($z/d = 0.0$, $y/d \approx 1.4$), and traversing around the plume in a counterclockwise direction, the plume boundary is expected to have wrapped down and around the wake region, dipping closer to the wall in the region where the boundary layer thinned ($z/d \approx 1.0$).[11] Although, the exact lateral extent of the plume is not discernible, the "dog-ear" structure located near $z/d \approx 1.0$, $y/d \approx 1.5$ is indicative of the low-momentum boundary layer fluid induction into the right vortex associated with the counter-rotating vortex pair.[10,11] Symmetry about

the z-axis, to within the experimental uncertainty, was observed.

The Mach number contour for the detached-shock diamond injectors are also in Figs. 4.7. The overall interpretation of these images is similar to that of the attached shocks. The notable differences are (1) the interaction shock extended about further into the freestream; (2) the shock shapes had more curvature, which is consistent with a detached bow shock, and (3) the low-Mach upwash region was significantly larger indicative of the increased mass flow rate and penetration

The Mach number contour for the circular injector is given in Figs. 4.7, where the features are very similar to the detached diamond injectors. However, the penetration of the interaction shock was approximately 10% lower than that for corresponding 90-degree diamond injector. Also, the circular injector low-Mach upwash region was significantly smaller than that for the diamond injector. However, the "dog-ear" structures at $z/d \approx \pm 1.0$, $y/d \approx 1.5$ are more pronounced for the circular injector, which indicates stronger plume vorticity.

Pressure Sensitive Paint

Pressure Sensitive Paint (PSP) data were acquired for all of the no-ramp conditions listed in Table 3.2; the results are summarized in Fig. 4.8. The pressure distributions reflect the flow topologies described with surface oil flows described earlier. Focusing on the low-pressure, 45° injector as a representative attached shock case, the pressure ratio (p/p_∞) increased to approximately 2.3 across the interaction shock. The surface pressure subsequently decreased through an expansion as the flow wrapped around the injected

fluid to a relatively low wake pressure, $p/p_\infty \approx 0.3$; this low pressure was expected.[8] For a representative detached diamond injector case, consider the high-pressure, 90° injector surface pressure distribution. For this case, the horseshow vortex, the high-pressure structure that wrapped around the injector, was a dominant high-pressure flow structure. The peak pressure ratio within the horseshoe vortex was approximately 4.2. The pressure ratio in the wake, just downstream of the injection port was nominally 0.3. The surface pressure field for the circular injector contained the same structures as for the corresponding 90-degree diamond injector. However, the shock standoff distance was significantly larger (123%) than for the corresponding diamond flow. The peak pressure ratio for the high-pressure circular injector was 4.9; the minimum pressure ratio in the wake was 0.15. The effective backpressure was measured from the surface pressure plots as the average pressure around the periphery (within approximately 0.2d of the injector edges) of the injector; the resulting ratios (λ) from this analysis are listed in Table 4.1.

Table 4.1 Performance Summary

α[a] (°)	y_p/d	λ	p_f/p_{eb}	Π
10.0	1.9	1.2	7.0	0.99
27.5	2.6	1.3	7.5	0.95
45.0	3.0	1.6	6.3	0.89
90.0	3.4	2.0	5.4	0.78
90.0[b]	**3.3**	**2.0**	5.4	0.71
10.0	2.5	1.4	29.4	0.94
27.5	3.5	1.7	26.8	0.84
45.0	4.1	1.7	27.3	0.74
90.0	4.7	2.0	23.4	0.70
90.0[b]	**4.8**	**2.2**	21.5	0.69

[a]First five entries correspond to P_{tj} = 0.10MPa (±1.0%); the second five correspond to P_{tj} = 0.46 MPa (±3.0%), [b]Circular Injector

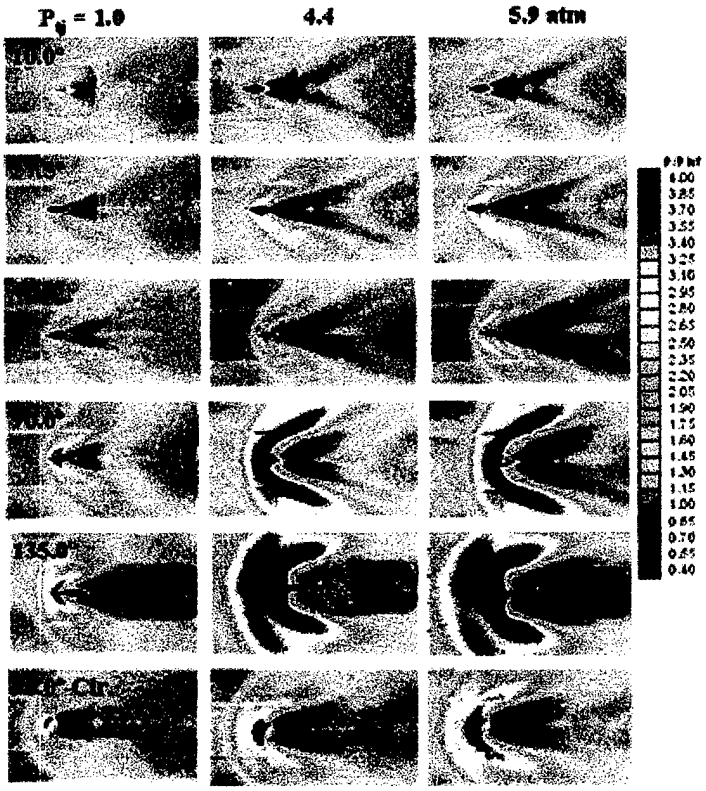

Fig. 4.8 PSP Summary

For perpendicular injection through circular orifices, the initial jet penetration has been shown to be strongly dependent on the p_j/p_{eb}.[24] Hence, that pressure ratio was also computed and included in Table 4.1. As indicated, for each of the two constant total pressure data sets, p_j/p_{eb} decreased by 25-30% as α increased from 10 to 90°. It is expected[24] that this decrease worked to decrease the initial penetration, and thus counteracted a portion of the penetration increase that would have resulted from the increase in J_{eff} that resulted from the increase in incidence angle.

Centerline pressure traces for all of the cases in Table 2 were obtained from the PSP

measurements and are plotted in Fig. 4.9. The leading edge of the injector was at x/d = 0.0. The trailing edge of the diamond and circular injectors were at x/d = 2.4 and 1.0, respectively. The peak pressure just upstream of the injector for the detached cases and a given geometry, increased with increasing injector pressure. For a given pressure ratio, the 90° circular injectors produced larger peak pressures than did the 90° diamond injector, indicating stronger shocks for the circular injectors. Standoff distances for the detached shock waves as estimated from this figure are summarized in Table 2. The standoff distance increased with both injector pressure and incidence angle, and was largest for the circular injector. The wake pressure traces, from just downstream of the injector ports to x/d ≈ 3.5, for all but the low-pressure 10° diamond injector, were similar in magnitude and shape. The low-pressure, 10°, diamond injector had a very low discharge coefficient, and hence the overall flow disturbances were small. The gap in the data between x/d = 3.5 to 5.0 was the result of a imperfection in the paint coverage due to the sealing of a port in the floor; this port is clearly visible in the contours shown in Fig. 8. Downstream of this region, the flow was compressed, and subsequently relaxed back to nearly the freestream pressure.

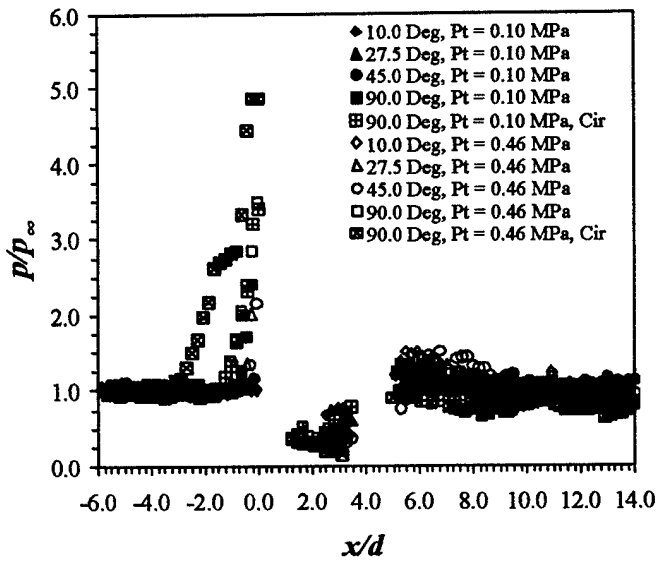

Fig. 4.9 Centerline Pressure Traces

Approximate Shock Loss Analysis

In order to estimate the bow shock total pressure loss, the three-dimensional interaction shock shape was modeled from the surface shock shape, the center plane shock shape, and cross-sectional shock shape. The cross-sectional shock shape was estimated from the five-hole probe, low-pressure Mach number data at x/d = 8.0. The cross sectional jet interaction shock shapes, nondimensionalized by the maximum y, z coordinates, at x/d = 8.0, were fit with the following 3rd order polynomial $y/y_{max} = a(z/z_{max})^3 + b(z/z_{max})^2 + c(z/z_{max}) + d$, where the coefficients a-d were found by applying boundary conditions at $z/z_{max} = 0$ and $z/z_{max} = 1$. The best agreement to the data was achieved with the following boundary conditions: At $z/z_{max} = 0$, $y/y_{max} = 1$ and $d(y/y_{max})/d(z/z_{max}) = -0.4$. At $z/z_{max} = 1$, $y/y_{max} = 0$ and $d(y/y_{max})/d(z/z_{max}) = -0.3$. The

mean square errors for all cases varied from 4.0 - 7.0%. The shock shape along the tunnel surface [i.e., $z_{max}(x/d)$] was evaluated from the data in Figs. 4.3 and 4.8. The centerline shock shape [i.e., $y_{max}(x/d)$] was directly measured from the shadowgraph photographs (Fig. 4). With the 3-D shock shape modeled, the unit normal vector ($\hat{n}$) to the shock surface was calculated by computing the gradient to the shock shape function. With the unit normal, the normal component of the Mach number over the shock surface was found by the relation $M_n = M_1 \hat{i} \cdot \hat{n}$. Because the jet was introduced into the tunnel boundary layer, M_1 was evaluated as a function y/d using the Van Driest II compressible turbulent velocity profile scaling.[23] The shock total pressure was then estimated with the normal component of the Mach number using normal shock theory.[20] The resulting area averaged total pressure losses, that is

$$\Pi = \frac{\iint_S \frac{p_{t2}}{p_{t1}} ds}{\iint_S ds} \tag{4.1}$$

were computed for $x/d \leq 8$, where S is the shock surface area, and the integrand in the numerator is a function of M_n for air. The results are listed in Table 2. For the high-pressure cases, the normalized shock cross-section fit was assumed. In order to quantify the scatter due to the curve fit, the shock loss was also calculated for the 45° case using two additional curves that defined upper and lower bounds in the experimental data for the scaled cross sectional shock fit. The resulting uncertainty was approximately ±4.0%. The shock loss data in Table 4.1 demonstrate that losses decreased with decreasing jet

incidence angle and injection pressure. The largest pressure losses were incurred by the 90°, circular injector.

4.2 Numerical Results (GASP v 4.1)

The numerical results obtained with the GASP code, as described in Chapter 3, are discussed in this section. The salient parameters described above provide the frame work for the initial discussion. However, the last two topics describe important results that do not have experimental counterpart data.

Separation Distance

The second column of Table 4.2 lists the computed separation distances normalized by the effective diameter of the jet. The results indicate that the separation distance increases with increasing J and increasing angle of incidence α. The 27.5°, low momentum case produces an attached shock while all other shocks are detached. Experimental results show that in both the 27.5° and 45°, low momentum case and 27.5°, high momentum case the shocks are attached. Figure 4.10 shows the representative numerical oil smear images for all the momentum ratios, for the 45° injection case. The freestream flow is from right to left in the figure. The jet interaction shock is shown clearly for all three momentum ratio cases. It is at the location where the freestream fluid deviates from the main flow direction. The shock standoff distance increases with increase in the momentum ratio. The leading edge horseshoe vortex angle also increases

with increase in the momentum ratio. This leads to an increase in the reattachment distance as indicated in the figure. Also, there is an increase in the lateral distance between the tunnel centerline and the outer boundary of the leading edge horseshoe vortex. This increase is also noted in the *Lateral Penetration* section. The separation between the wake vortices also increases with increasing momentum ratio. The trend of increasing shock separation distance with increase in momentum ratio is observed in all cases.

Table 1.2 Numerical Simulation Results.

α^a (deg)	Δ/d^b	y_p/d^c	Π	y_p/d^c *% Error*	Π% *Error*
27.5	*AS*	2.10	0.93	19.23	2.11
45	0.19	3.00	0.88	0.00	1.12
90	0.70	2.00	0.80	41.18	2.56
135	2.00	1.85	0.85	NA	NA
27.5	0.26	4.24	0.80	21.14	4.76
45	0.46	5.36	0.68	30.73	8.11
90	1.90	3.30	0.47	29.79	32.86
135	6.80	3.22	0.50	NA	NA
27.5	0.30	4.75	0.76	NA	NA
45	0.58	5.63	0.62	NA	NA
90	3.60	4.10	0.39	NA	NA
135	9.75	4.08	0.44	NA	NA

[a]First four entries correspond to P_{tj} = 0.10MPa; the second four correspond to P_{tj} = 0.46 MPa; the third four correspond to P_{tj} = 0.63 MPa, [b]AS = Attached Shock, [c]x/d = 7.5, NA=Not Applicable

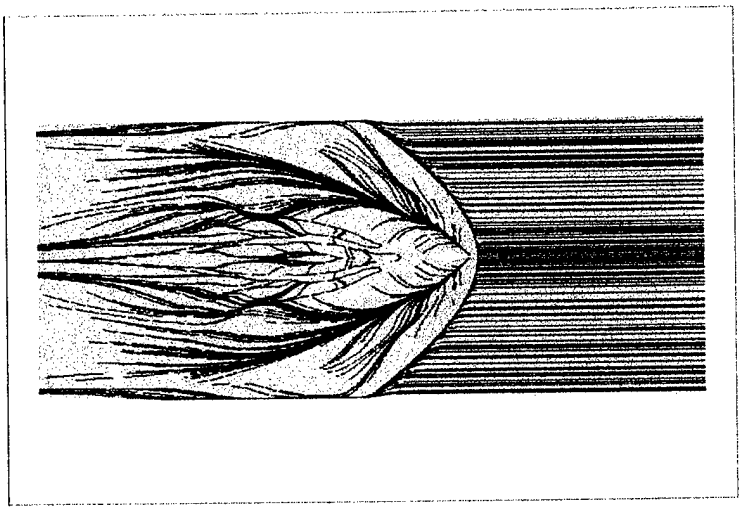

b. P_{tj} = 0.46 MPa

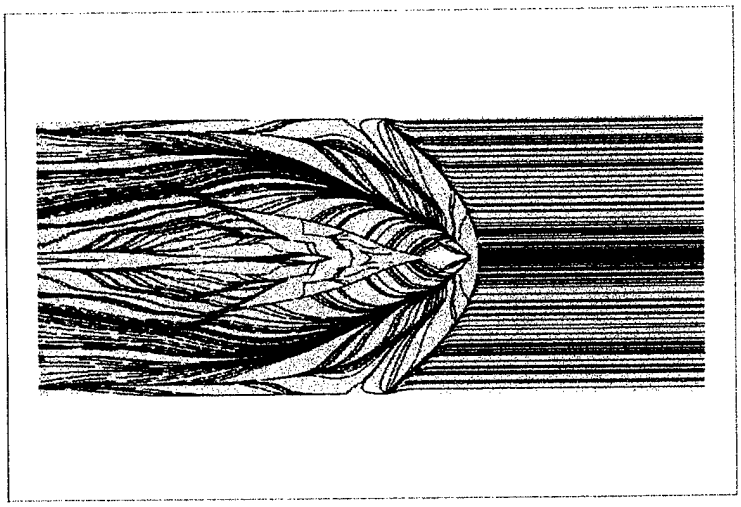

c. P_{tj} = 0.63 MPa

Fig. 4.10 45° Injection –Numerical Oil Smear.

Normal Penetration

The experimental penetration data at $x/d = 7.5$ listed in Table 4.1 indicates that the penetration increased with increasing angle of incidence and increasing momentum ratios. Normal penetration of the injectant fluid in the current simulation was measured

by projecting the injectant streamlines on the symmetry plane of the tunnel. Figure 4.11 shows the injectant streamlines for the 45° cases. The cross plane is at a location of $x/d = 7.5$. Both the cross plane and the streamlines are colored with Mach number values. The penetration height was taken at the streamline with the highest y/d value. The data summarized in Table 4.2 indicated that the penetration distance increases by almost 80 percent when the total pressure of the jet increases from 0.1 MPa to 0.46 MPa. However the increase in jet total pressure from 0.46 MPa to 0.63 MPa results in only a 5 percent increase in penetration. A similar trend is observed in the 27.5° case.

Lateral Penetration

Figure 4.12 shows the lateral penetration of the injectant fluid streamlines. It is observed that although the penetration in the normal direction seems considerably higher for the high jet total pressure cases, it is not as uniform as the low jet total pressure case. The lateral penetration shows a marked increase as the jet total pressure is increased and the penetration is more uniform when compared with the normal penetration. Also, clear increase in the normal and lateral penetration is noted as the jet total pressure is further increased to 0.63 MPa.

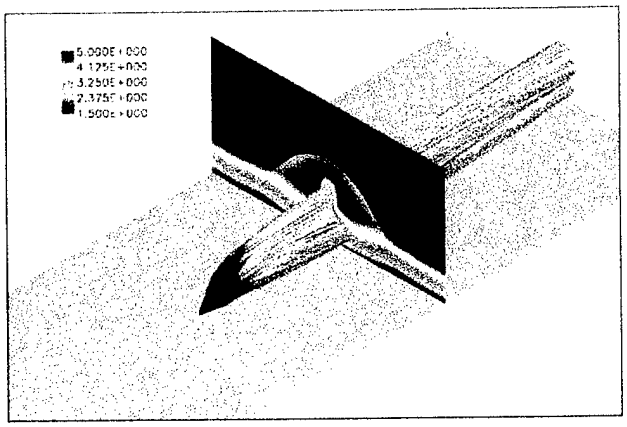

a. P_{tj} = 0.1 MPa

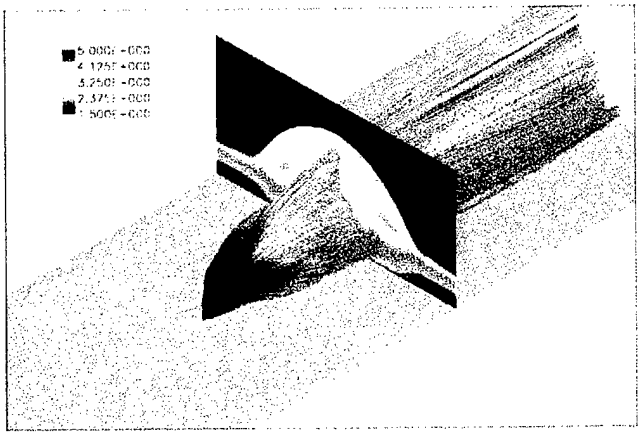

b. P_{tj} = 0.46 MPa

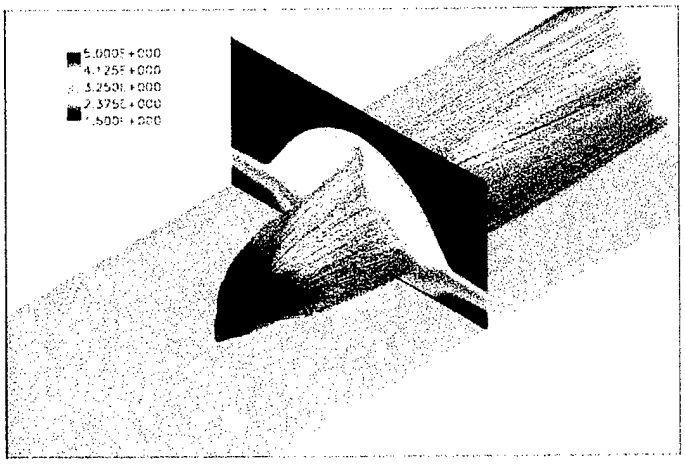

c. P_{tj} = 0.63 MPa

Fig. 4.11 45° Injection – Injectant Streamlines.

(a) P_{tj} = 0.1 MPa (b) P_{tj} = 0.46 MPa (c) P_{tj} = 0.63 MPa
Fig. 4.12 45° Injection – Injectant Streamlines Showing Lateral Penetration.

Figures 4.13-4.15 show the injectant streamlines for the 27.5°, 90°, and 135° cases. The core of the jet fluid penetrates less laterally in the 27.5° cases as compared to the 45° cases. It is seen that the 27.5° injection follows a trend similar to the 45° cases with increase in jet total pressure. The 90° and 135° injection cases show marked increase in lateral penetration, especially at higher momentum ratios. The injectant travels far upstream in the 135°, high momentum ratio case as seen in Fig. 4.15b. This is not observed in other cases.

Total Pressure Loss

Total pressure loss parameter [Eq. (4.1)] was calculated for all the cases. A plane at station $x/d = 8.0$, spanning z/d = -4 to +4 and y/d = 0 to 7 was used for evaluating the total pressure after the shock. The resulting values are listed in Table 4.2. It is seen that as the angle of incidence increases from 27.5° to 90° the total pressure loss increases. This closely parallels the experimental results in Table 4.1. This increase in total pressure loss can be attributed to stronger shocks that are produced as the injector angle increases. The difference between the experimental and numerical total pressure loss increases for cases where the jet total pressure is 0.46 Mpa.

The 135° injection cases' total pressure loss is less than that of the 90° cases. This is contrary to the expected result since a 135° injection should result in a stronger shock. Additional investigation into this phenomenon needs to be performed.

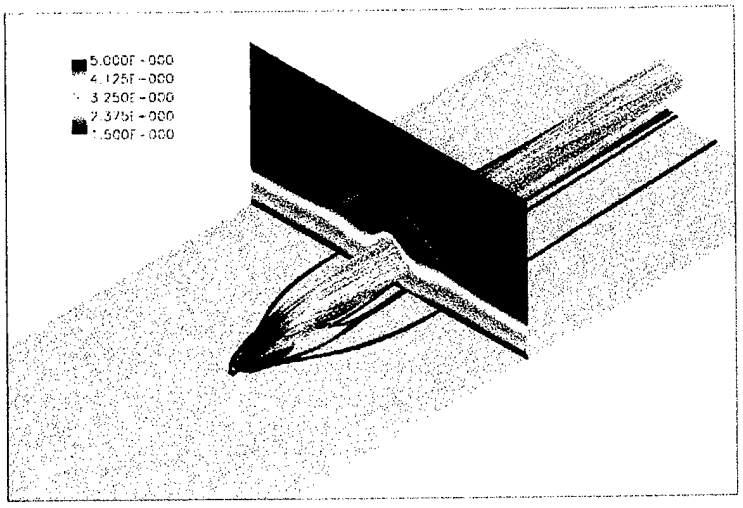

a. P_{tj} = 0.1 MPa

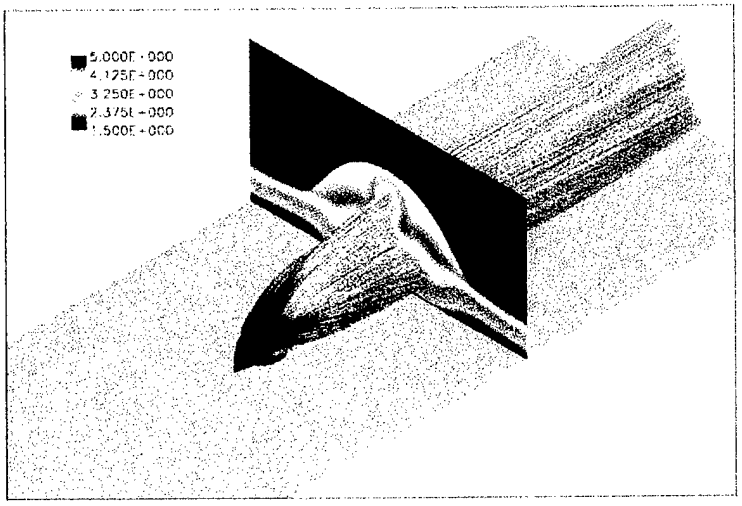

b. P_{tj} = 0.46 MPa

Fig. 4.13 27.5° Injection – Injectant Streamlines.

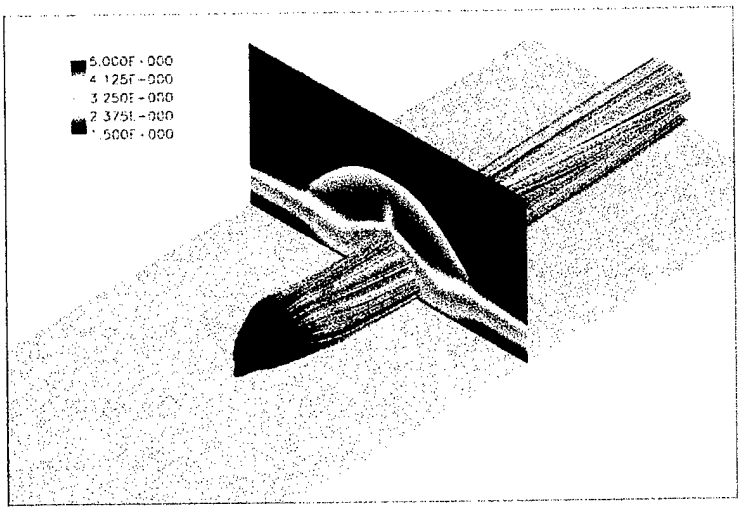

a. P_{tj} = 0.1 MPa

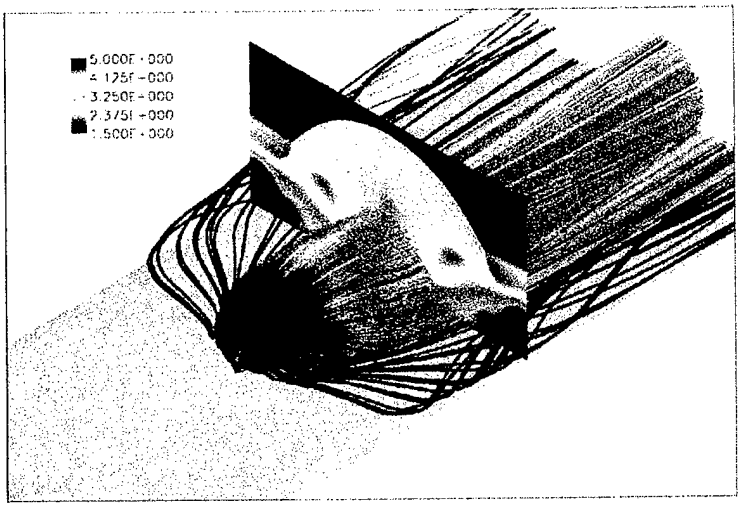

b. P_{tj} = 0.46 MPa

Fig. 4.14. 90° Injection – Injectant Streamlines.

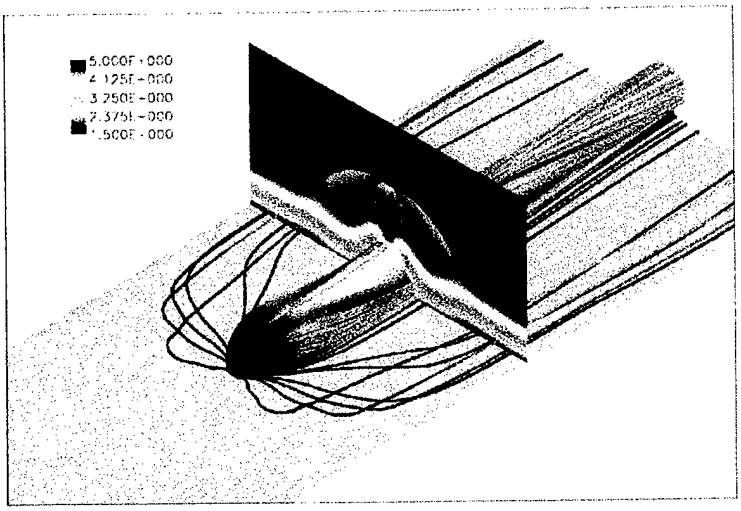

a. P_{tj} = 0.1 MPa

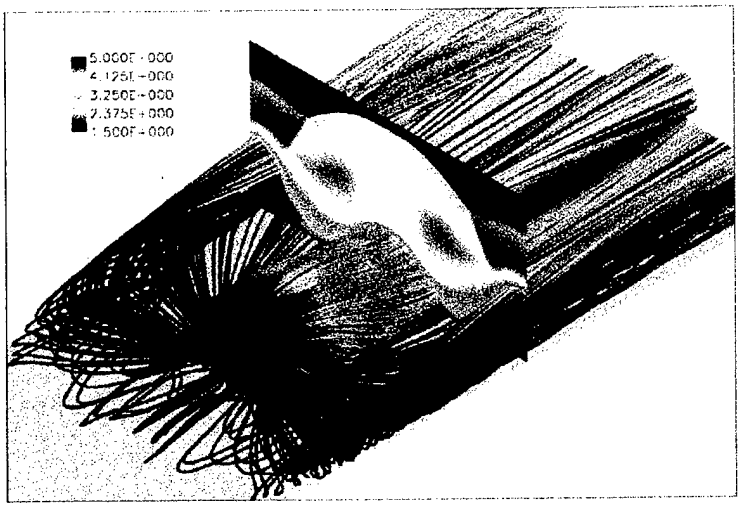

b. P_{tj} = 0.46 MPa

Fig. 4.15 135° Injection – Injectant Streamlines.

Vortex Structures

The transverse jet interaction flow field is dominated by numerous vortices as described in Chapter 2 In addition to previously documented vortices, a new vortex mechanism is observed in the current simulations. Figure 4.16 shows the vortex cores

[Haimes and Kenwright (1999), Sujuki and Haimes (1995)] in the flow field. Starting from the bottom left corner of the figure and moving to the top right corner we first encounter the vortex core for the shock separation vortex. Above the trailing edge of the jet are the vortex cores for the newly identified transverse counter rotating vortex pair (TCVP). Starting near the TCVP are the vortex cores for the wake vortices. The reattachment vortex cores start near the trailing edge of the jet.

Figure 4.17 shows some of the vortices associated with the cores discussed previously. The leading edge shock separation vortex is clearly visible at the bottom left corner of the figure. Moving along a diagonal path we encounter the TCVP. This vortex pair is formed as the incoming boundary layer fluid, which is transported into the upper layers, interacts with the fluid issuing from the jet exit.

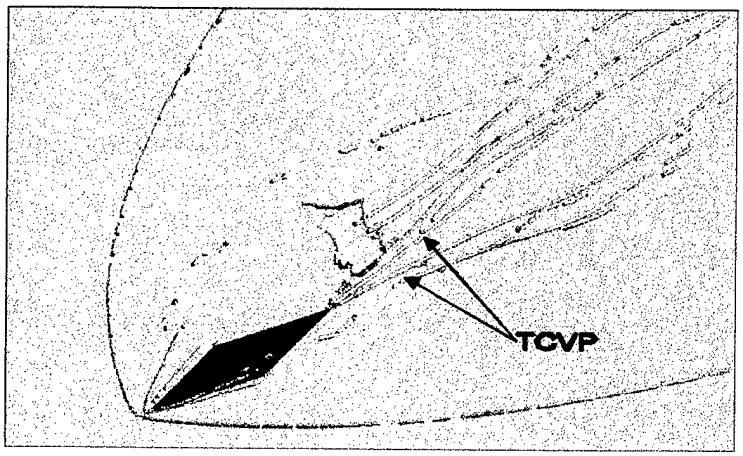

Fig. 4.16 Vortex Cores

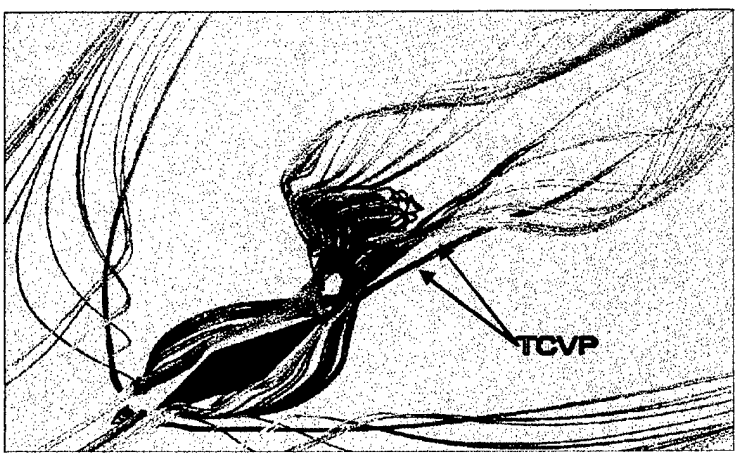

Fig 4.17 Transverse Counter Rotating Vortex Pair.

Chapter 5

Conclusions

5.1 Experimental Conclusions

An experimental study to characterize the near-field ($x/d < 8.0$) flow for gaseous injection through diamond shaped orifices (15° half angle) at four incidence angles (10, 27.5, 45 and 90°) and three total pressures (P_{tj} = 0.10, 0.46 and 0.63 MPa) into a high Reynolds number (Re/m = 53 x 10^6) Mach 5.0 freestream was performed. A 90° circular injector, with the same exit port area and total pressures, was examined for comparative purposes. Flow control ramps [Wilson, Bowersox and Glawe (1998)] were investigated to quantify the effect on plume vorticity. The experimental methods included surface oil flow visualization, shadowgraph photography, Mie-scattering flow visualization, pressure sensitive paint (PSP) and a Pitot-cone five-hole pressure probe. Flowfield documentation, jet penetration and shock induced total pressure loss were derived from these data. From these data, the following specific conclusions were drawn. First, near-wall attachment of the jet interaction shock wave depended on both incidence angle and injector pressure, where the shock remained attached at higher incidence angles at the lower injection pressure. Second, δ/d = 1.6; hence, the detached shocks separated the incoming boundary layer and generated the familiar lambda shock structure. Lambda shocks were not observed for the attached shock cases. Third, near-field, $x/d < 8.0$, centerline penetration correlations $y_p/d = f_p(\xi)$, where $\xi = J_{eff}^{m}(x/d)^n$, were developed for both the

diamond and circular injectors; f_p was hyperbolic and linear for the diamond and circular injectors, respectively. Fourth, for the detached cases, the highest surface pressures were associated with the horseshoe vortex. Fifth, the upstream peak pressures for the detached cases, for a given injector geometry, increased with increasing injector pressure. Sixth, for a given pressure ratio, the 90° circular injectors produced largest peak pressures. Seventh, the shock induced total pressure losses decreased with decreasing jet incidence angle and injection pressure, where the largest losses were incurred by the 90°, circular injector.

5.2 Numerical Conclusions

Numerical simulations were performed for sonic injection through diamond orifices into a Mach 5.0 freestream. Four different injector angles (27.5°, 45°, 90° and 135°) and three total pressures (0.1, 0.46 and 0.63 MPa) resulting in a total of 12 cases were executed. The derived data from these simulations were compared to experimental results. Although some of the data compared well with experimental results, there were significant differences in other cases. Shock separation distance was found to depend on the jet incidence angle and the jet total pressure. Increasing angle of incidence and increasing total pressure led to larger shock standoff distances. Penetration was found to be highest for the 45° injection as compared to the 90° case (experimental). But the 90° injection case penetration was found to be more uniform as compared to the 45° case. Lateral penetration results indicated that higher jet total pressures results in more lateral penetration of the injectant fluid. Injectant in the high momentum ratio, 135° case

reached far upstream of the injector location. Total pressure loss follows experimental trends for the 27.5°, 45° and the 90° cases while the total pressure loss for the 135° cases is less compared to the 90° cases. Vortex core plots showed the existence of a transverse counter rotating vortex pair immediately downstream of the jet.

5.3 Ongoing Calculations

High-fidelity numerical simulations are continuing at Texas A&M University using Mentor's SST model with detached eddy simulation The focus of these simulations is improved understanding of the vorticity dynamics and the controllability of the secondary flow motion using gas dynamic actuation. Computer support for these simulations is being provided by the Air Force ASC HPC. Student support for analyzing the numerical data is being provided by Texas A&M University. The results from these simulations will be reported to the Air Force and AFOSR at a later date.

Bibliography

Aerosoft, Inc., *GASP Version 3 Users' Manual,* Blacksburg, VA, 1999.

Abromovich, G., *The Theory of Turbulent Jets,* MIT Press, Cambridge, MA, 1960.

Andreopoulos, J. and Rodi, W., "Experimental Investigation of Jets in a Cross-flow," *J. Fluid Mech.*, Vol. 138, 1984, pp. 93-127.

Anderson, J., *Modern Compressible Flow with Historical Perspective, 2nd Ed.*, McGraw Hill, New York, 1990.

Alverez, J., Jones, W., and Seoud, R., "Predictions of Momentum and Scalar Fields in a Jet in a Cross-flow using First and Second Order Turbulence Closure," AGARD-CP-534, 1993, pp. 24.1-24.10.

Bowersox, R, Tucker, K., and Whitcomb, C., "Two-Dimensional Nonadiabatic Injection into a Supersonic Freestream," *Journal of Propulsion and Power,* March-April, 2000, pp. 234-242.

Bowersox, R., "Thermal Anemometry," *Handbook of Fluid Dynamics and Fluids Machinery,* ed. J. Schetz and W. Fuhs, John-Wiley, New York, 1996a, pp. 965-983.

Bowersox, R., "Combined Laser Doppler Velocimetry and Cross-Wire Anemometry Analysis for Supersonic Turbulent Flow," *AIAA J.,* Vol. 34, No. 11, 1996b, pp. 2269-2275.

Bowersox, R., "Turbulent Flow Structure Characterization of Angled Injection into a Supersonic Cross-flow," *J. of Spacecraft and Rockets,* Vol. 34, No. 2, 1996c, pp. 205-213.

Chenault, L., Beran, P., and Bowersox, R. "Numerical Investigation of Supersonic Injection Using a Reynolds-Stress Transport Model," *AIAA Journal*, Vol. 37, No. 10, 1999, pp. 1257-1269.

Chui, S., Karling, R., Margason, R., Tso, J., "A Numerical Investigation of a Subsonic Jet into a Cross-flow," AGARD-CP-534, 1993, pp. 22.1-22.14.

Drummond, P., "Suppression and Enhancement of Mixing in High-Speed Reacting Flow fields," *Combustion in High-Speed Flows*, Kluwer Acad. Press., 1994, pp. 191-229.

Fric, T. F. and Roshko, A., "Structure in the Near Field of the Transverse Jet," Proceedings of the Seventh Symposium on Turbulent Shear Flows, Vol. 1 (A90-35176), Aug. 1989, pp. 6.4.1-6.4.6.

Fric, T. and Roshko, A., "Vortical Structure in the Wake of a Transverse Jet,"*JFM*, Vol. 279, pp. 1-47. General Discussion, AGARD-CP-523, 1993, pp. GD.1-GD.13.

Fuller, E., Mays, R., Thomas, R., Schetz, J., "Mixing Studies of Helium in Air at High Supersonic Speeds," *AIAA Journal*, Vol. 30, No. 9., 1992, pp. 2234-2243.

Gessner, F., "The Origin of Secondary Flow in Turbulent Flow Along a Corner," *J. of Fluid Mechanics*, Vol. 58, Part 1., 1973, pp. 1-25.

Grasso, F., and V. Magi, "Simulation of Transverse Gas Injection in Turbulent Supersonic Air Flows", *AIAA Journal*, Vol. 33, No. 1, 1995, pp. 56-62.

Haimes, R. and Kenwright., D., "On the Velocity Gradient Tensor and Fluid Feature Extraction," AIAA Paper 99-3288, 1999.

Hinze, O., *Turbulence*, McGraw-Hill, 1975.

Hirsch., C., *Numerical Computation of internal and External Flows*, Volumes 1 and 2.,

John Wiley and Sons, New York, 1992

Holeman, J., *Heat Transfer 6th Ed.*, McGraw-Hill, New York, 1986.

Hollo, S. D., J. C. McDaniel and R. J. Harfield, "Quantitative Investigation of Compressible Mixing: Staged Transverse Injection into Mach 2 Flow", *AIAA Journal*, Vol. 32, No. 3, 1994, pp. 528-534.

Kamotani, Y. and Greber, I., "Experiments on a Turbulent Jet in a Cross-flow," *AIAA J.*, Vol. 10, No. 11, 1972, pp. 1425-1429.

Kelso, R., Delo, C, and Smits, A., "Unsteady Wake Structures in Transverse Jets," AGARD-CP-534, 1993, pp. 4.1-8.

Keuthe, A. M., "Investigation of the Turbulent Mixing Regions Formed by Jets," *J. of Appl. Mech.*, Sept. 1935, pp. A-87-A-95.

Kovasznay, L., "Hot-Wire Anemometry in Supersonic Flow," *J. of Aeron. Sci.*, Vol. 17, 1950, pp. 565-584.

Lozano, A., Smith, S., Mungal, M., Hanson, R., "Concentration Measurements in a Transverse Jet by Planar Laser Induced Fluorescence of Acetone," *AIAA J.*, Vol. 32, 1994, pp. 218-221.

Margason, R. J., "Fifty Years of Jets in Cross-flow Research," AGARD-CP-534, Nov. 1993, pp. 1.1 - 1.41.

McCann, G. and Bowersox, R., "Experimental Investigation of Supersonic Gaseous Injection into a Supersonic Free stream," *AIAA J.*, Vol. 34, 1996, pp. 317-323.

Morrison, J., "A Compressible Navier-Stokes Solver with Two-Equation and Reynolds Stress Turbulence Closure," NASA CR-4440, May 1992.

Roe, P. L., "Approximate Riemann Solvers, Parameter Vectors, and Difference Schemes," *Journal of Computational Physics*, Vol. 43, 1981, pp. 357-372.

Schetz J. A. and F. S. Billig, "Penetration of Gaseous Jets Injected into a Supersonic Stream", *Journal of Spacecraft and Rockets*, Vol. 3, No. 11, 1966, pp. 1658-1665.

Spangenberg, W., "Heat Loss Characteristics of Hot-Wire Anemometers at Various Densities in transonic and Supersonic Flow," NACA TN 3381, 1955.

Sujuki, D. and Haimes, R., "Identification of Swirling Flow in 3-D Vector Fields," AIAA Paper 95-1715, 1995.

United States Air Force, *New World Vistas, Air and Space Power for the 21st Century, Aircraft and Propulsion Volume,* 1995.

Wilcox, D. C., *Turbulence Modeling for CFD*, DCW Inc., La Canada, CA, 2000.

Wilson, M., Bowersox, R., and Glawe, D., "An Experimental Investigation of the Role of Downstream Ramps on a Supersonic Injection Plume," *Journal of Propulsion and Power,* Vol. 15, No. 3, 1998, pp. 432-439.